

Multi-band effects on Fulde-Ferrell-Larkin-Ovchinnikov states of Pauli-limited superconductors

Masahiro Takahashi,^{1,*} Takeshi Mizushima,^{2,†} and Kazushige Machida^{2,‡}

¹*Department of Physics, Gakushuin University, Tokyo 171-8588, Japan*

²*Department of Physics, Okayama University, Okayama 700-8530, Japan*

(Dated: March 11, 2022)

Multi-band effects on Fulde-Ferrell-Larkin-Ovchinnikov (FFLO) states of a Pauli-limiting two-band superconductor are studied theoretically, based on self-consistent calculations of the Bogoliubov-de Gennes equation. First, we examine the phase diagrams of two-band systems with a passive band in which the intraband pairing interaction is absent and superconductivity is induced by a Cooper pair tunneling from an active band. It is demonstrated that the temperature of the Lifshitz point at which three second-order transition lines meet is independent of the Cooper pair tunneling strength. The BCS-FFLO critical field becomes lower than the Lifshitz point with increasing the interband tunneling strength, and the resultant phase diagram is qualitatively different from that in a single-band superconductor. We also study the thermodynamics of Pauli-limiting two-band superconductors with comparable intraband pairing interactions. As a consequence of a competing effect between two bands, the FFLO phase is divided into two phases: Q_1 - and Q_2 -FFLO phases. The Q_1 -FFLO is favored in a high field regime and the Q_2 -FFLO becomes stable in the lower field. In a particular case, the latter is further subdivided into a family of FFLO states with rational modulation lengths, leading to a devil's staircase structure in the field-dependence of physical quantities. The critical field, above which the FFLO is stabilized, is lower than that in a single band superconductor, while the temperature of tricritical Lifshitz point is invariant under the change of two-band parameters.

PACS numbers: 74.20.-z, 74.25.Dw, 74.81.-g

I. INTRODUCTION

There have been intensive interests in the realization of Fulde-Ferrell-Larkin-Ovchinnikov (FFLO) states in superconductors under a high magnetic field, since the first theoretical prediction.^{1,2} Studies on FFLO states have been expanded into various fields, ranging from condensed matter³ and cold atoms⁴⁻⁹ to neutron stars.¹⁰ Although several candidates for FFLO superconductors have already been proposed by numerous works, direct evidence of FFLO states has not been observed in experiments.

In a Pauli-limited superconductor, the transition from the Bardeen-Cooper-Schrieffer (BCS) state to the FFLO state is considered as the second-order transition accompanied by the Jackiw-Rebbi soliton¹¹ which neatly accommodates Pauli paramagnetic moment.¹² The soliton provides a generic key concept for commonly understanding the essential physics of FFLO phases in a single-band superconductor, incommensurate structures,^{13,14} and fermionic excitations bound at topological defects of a superconductor through π -phase shift of the background fields.¹⁵

Multi-band effects originating from multiple sheets of Fermi surfaces have recently been observed in a variety of superconductors, such as MgB₂, iron-based superconductors, and Sr₂RuO₄.^{16,17} Among them, strong Pauli effects have been reported in iron-pnictides.¹⁸⁻²⁴ It is now recognized that multi-band effects are crucial to understand unconventional superconductivity. Nevertheless, in contrast to extensive studies in single-band supercon-

ductors,³ the structure and thermodynamic stability of FFLO phases in multi-band systems have not been clarified so far other than a few exception.²⁵⁻²⁷

The Pauli-limiting field H_p for a single-band system is given by $\mu_B H_p^{\text{single}} = \Delta_0 / \sqrt{2}$, which depends only on the gap, Δ_0 , at $T = 0$ and $H = 0$. This formula is easily extended to a two-band case as

$$\mu_B H_p^{\text{two}} = \sqrt{\frac{1}{2} \left(\frac{\mathcal{N}_F^{(1)}}{\mathcal{N}_F} [\Delta_0^{(1)}]^2 + \frac{\mathcal{N}_F^{(2)}}{\mathcal{N}_F} [\Delta_0^{(2)}]^2 \right)}, \quad (1)$$

where $\mathcal{N}_F^{(\gamma)}$ ($\Delta_0^{(\gamma)}$) is the density of states (gap) for the γ band ($\gamma = 1$ or 2) and we introduce $\mathcal{N}_F = \mathcal{N}_F^{(1)} + \mathcal{N}_F^{(2)}$. When the major gap $\Delta_0^{(1)}$ dominates the minor gap $\Delta_0^{(2)}$ ($\Delta_0^{(1)} \gg \Delta_0^{(2)}$), the Pauli-limiting field in the case of two-band systems, $\mu_B H_p^{\text{two}} \simeq \sqrt{\mathcal{N}_F^{(1)} / \mathcal{N}_F} [\Delta_0^{(1)} / \sqrt{2}]$, is smaller than $\mu_B H_p^{\text{single}} = \Delta_0^{(1)} / \sqrt{2}$. For $\mathcal{N}_F^{(2)} \gg \mathcal{N}_F^{(1)}$, Eq. (1) reduces to $\mu_B H_p^{\text{two}} \simeq \Delta_0^{(2)} / \sqrt{2} = \mu_B H_p^{(2)} < \mu_B H_p^{(1)}$ with $H_p^{(\gamma)}$ being the Pauli-limiting field for the γ band. These two limiting cases show that the FFLO region could become enlarged towards the lower field. This simple consideration motivates us to look into the Pauli paramagnetic effects in multi-band superconductivity.

The FFLO states are Cooper pairing states with a finite center-of-mass momentum Q . The nonzero center-of-mass momentum generates a spatial modulation of Cooper pair amplitudes in real space, *e.g.*, $\Delta(z) \propto \sin(Qz)$. The modulation period $2\pi/Q$ is determined by

competing effect between spin paramagnetism and superconductivity. For a single-band case, the analytic form of the modulation length is derived in Ref. 12. At zero temperature, the modulation length depends on the amplitude of the pair potential at zero field, the Fermi wavelength of background electrons, and an external field. In the case of a two-band superconductor, each band has its own favorable value of the modulation period, $2\pi/Q^{(1)}$ and $2\pi/Q^{(2)}$. The competing and synergetic effect arises from a coherent coupling of two bands having two modulation periods $2\pi/Q^{(1)}$ and $2\pi/Q^{(2)}$ through interband Cooper pair tunneling, which makes the phase diagram of FFLO states rich and complex. We also note that multi-band effects might be accompanied by exotic superconductivity.^{28–32}

In the previous work,²⁷ it is found that in a Pauli-limiting two-band superconductor, the coherent coupling of two bands through the interband Cooper pair tunneling gives rise to a devil's staircase structure in the field dependence of physical quantities and a rich FFLO phase diagram. In this paper, we more extensively investigate the thermodynamic stability and electronic structures of Pauli-limiting two-band superconductors in a wide region of parameters. Based on self-consistent calculation of the Bogoliubov-de Gennes (BdG) equation, we first start to examine the phase diagram of a simplest two-band superconductor with a passive band in which the pairing interaction is absent and the superconductivity is induced by the Cooper pairing transfer from the active band. The resultant phase diagram is accompanied by the positive slope of the BCS-FFLO phase boundary line, $T_{LO}(H)$,

$$\frac{dT_{LO}(H)}{dH} > 0. \quad (2)$$

This is contrast to the phase boundary in a single-band superconductor, $dT_{LO}/dH < 0$ (see the solid line of Fig. 1 and Refs. 3 and 33). We investigate the phase diagram in the more general case that two bands with comparable intraband interactions are coherently coupled through the Cooper pair tunneling. It is demonstrated that the sequence of FFLO phases with rational modulation length is widely observed when the tunneling rate is present. For all parameters used in the current work, the tricritical Lifshitz point “L” is found to be a fixed point, $T_L/T_c = 0.56 \dots$.

This article is organized as follows. In the next section, we introduce the BdG equation for a multi-band system. The details of the derivation are supplemented in Appendix A. In Appendix B, we also describe the way to numerically solve the BdG equation with a periodic boundary condition. The analytic form for the phase boundaries between superconducting states and normal states is derived in the latter half of the section. In Sec. III, we consider a two-band superconductor with a passive band, where the interaction for intraband Cooper pairing formation is absent in the second (passive) band and the superconductivity is induced by the Cooper pair tun-

neling from the first (active) band. In Sec. IV, we show the numerical results on FFLO states of Pauli-limiting two-band superconductors, where both the bands have intraband pairing interaction. Finally, Sec. V is devoted to summary.

II. FORMULATION

A. Multi-band Bogoliubov-de Gennes equation

We start from the second-quantized microscopic Hamiltonian with multiple bands under a uniform external magnetic field. The Hamiltonian is given as

$$\mathcal{H} = \mathcal{H}_0 + \mathcal{H}_{\text{int}}, \quad (3)$$

where the single-particle Hamiltonian and interaction Hamiltonian are

$$\mathcal{H}_0 = \sum_{\gamma, \sigma, \sigma'} \int d\mathbf{r} \psi_{\sigma}^{(\gamma)\dagger}(\mathbf{r}) \underline{\xi}_{\sigma, \sigma'}^{(\gamma)}(\mathbf{r}) \psi_{\sigma'}^{(\gamma)}(\mathbf{r}), \quad (4)$$

$$\mathcal{H}_{\text{int}} = \sum_{\gamma, \gamma'} g_{\gamma\gamma'} \int d\mathbf{r} \psi_{\uparrow}^{(\gamma)\dagger}(\mathbf{r}) \psi_{\downarrow}^{(\gamma)\dagger}(\mathbf{r}) \psi_{\downarrow}^{(\gamma')}(\mathbf{r}) \psi_{\uparrow}^{(\gamma')}(\mathbf{r}). \quad (5)$$

The sums of σ, σ' are taken for up- and down-spins \uparrow, \downarrow , and electron bands are denoted by $\gamma = 1, 2, \dots, N$. The single-particle Hamiltonian density $\underline{\xi}_{\sigma, \sigma'}^{(\gamma)}$ is a (σ, σ') component of a two-dimensional matrix $\underline{\xi}^{(\gamma)}$,

$$\underline{\xi}^{(\gamma)}(\mathbf{r}) = \varepsilon^{(\gamma)}(\mathbf{r}) \underline{1}_2 - \mu_B^{(\gamma)} \mathbf{H} \cdot \underline{\sigma}, \quad (6)$$

with $\varepsilon^{(\gamma)}(\mathbf{r}) = \frac{\hbar^2}{2M_e^{(\gamma)}} (-i\nabla + \mathbf{A})^2 - \mu_{\gamma}$. The creation and annihilation field operators, $\psi_{\sigma}^{(\gamma)\dagger}$ and $\psi_{\sigma}^{(\gamma)}$, are defined for each band and spin state. The electron mass and effective Bohr magneton in the γ band are denoted as $M_e^{(\gamma)}$ and $\mu_B^{(\gamma)}$, respectively. The n -dimensional unit matrix is denoted as $\underline{1}_n$. We assume the effective coupling of electrons in the bands γ and γ' as $g_{\gamma\gamma'} = g_{\gamma'\gamma} (\leq 0)$. Here \mathbf{A} is a vector potential, μ_{γ} is a chemical potential of the γ band, and \mathbf{H} is an external magnetic field coupled with spins through $\underline{\sigma} = (\underline{\sigma}_x, \underline{\sigma}_y, \underline{\sigma}_z)$, where $\underline{\sigma}_{\alpha}$ ($\alpha = x, y, z$) are 2×2 Pauli matrices.

Employing the mean field approximation and following the usual procedure,³⁴ we have the following BdG equation for the quasiparticle wavefunction $\varphi_{\nu}^{(\gamma)}(\mathbf{r}) = [u_{\nu}^{(\gamma)}(\mathbf{r}), v_{\nu}^{(\gamma)}(\mathbf{r})]^T$,

$$\underline{\mathcal{K}}^{(\gamma)}(\mathbf{r}) \varphi_{\nu}^{(\gamma)}(\mathbf{r}) = E_{\nu}^{(\gamma)} \varphi_{\nu}^{(\gamma)}(\mathbf{r}), \quad (7)$$

where the 2×2 BdG matrix is

$$\underline{\mathcal{K}}^{(\gamma)}(\mathbf{r}) = \begin{bmatrix} \varepsilon^{(\gamma)}(\mathbf{r}) - \mu_B^{(\gamma)} H & \Delta^{(\gamma)}(\mathbf{r}) \\ \Delta^{(\gamma)*}(\mathbf{r}) & -\varepsilon^{(\gamma)}(\mathbf{r}) - \mu_B^{(\gamma)} H \end{bmatrix}. \quad (8)$$

Equation (7) is self-consistently coupled with the pair potential,

$$\Delta^{(\gamma)}(\mathbf{r}) = \sum_{\gamma'} \sum_{|E_{\nu}^{(\gamma')}| < E_c} g_{\gamma\gamma'} u_{\nu}^{(\gamma')}(\mathbf{r}) v_{\nu}^{(\gamma')*}(\mathbf{r}) f(E_{\nu}^{(\gamma')}), \quad (9)$$

where $f(E) = 1/(e^{E/k_B T} + 1)$ is the Fermi distribution function at a temperature T . Here, we assume that \mathbf{H} is fixed to the z axis without loss of generality. The detailed formalism is explained in Appendix A.

In this formalism, we take account of multi-band effects through the gap equation (9). The coupling constants, $g_{\gamma\gamma'}$, lead to the formation of intraband Cooper pairs, and $g_{\gamma\gamma'}$ ($\gamma \neq \gamma'$) induces the interband Cooper pair tunneling. Hence, in the case of nonzero $g_{\gamma\gamma'}$ ($\gamma \neq \gamma'$), multiple electron bands are coherently coupled with each other through the interband Cooper pair transfer. This multi-band effect is crucial for the sequence of FFLO phase transitions discussed in Sec. IV.

For simplicity and to stay in a minimal model, we consider a one-dimensional system along the z direction. Throughout this paper, the effective masses $M_e^{(\gamma)}$, and the effective Bohr magnetons $\mu_B^{(\gamma)}$ of electrons in each band are set to be the same, $M_e \equiv M_e^{(1)} = M_e^{(2)}$ and $\mu_B = \mu_B^{(1)} = \mu_B^{(2)}$, respectively. Since we are interested in the strong Pauli paramagnetic limit, the vector potential \mathbf{A} is supposed to be spatially uniform, neglecting the orbital depairing effect.³³ Note that the orbital depairing effect can be suppressed in low-dimensional superconductors.^{35,36}

We numerically solve the self-consistent equations (7) and (9). We consider a one-dimensional modulation of the pair potential with the period L ,

$$\Delta^{(\gamma)}(z + L/2) = e^{i\chi} \Delta^{(\gamma)}(z), \quad (10)$$

where $\chi = \pi$ (2π) corresponds to FFLO (BCS) states. The period L determines the FFLO modulation wavenumber Q ,

$$Q \equiv 2\pi/L. \quad (11)$$

This imposes the periodic boundary condition on the quasiparticle wave functions,

$$\varphi_{\nu}^{(\gamma)}(z + pL/2) = e^{ikR} e^{i\chi\sigma_z/2} \varphi_{\nu}^{(\gamma)}(z), \quad (12)$$

where $k = \frac{2\pi q}{LN_L}$ is the Bloch vector and R denotes the Bravais lattice vector $R = pL/2$ in the one-dimensional system, which satisfies $kR = \pi pq/N_L$ with $p, q, N_L \in \mathbb{Z}$. We numerically diagonalize the BdG equation (7) with the periodic boundary condition by using a finite element method implemented with the Gauss-Lobatto discrete variable representation. The details are described in Appendix B.

Using the self-consistent solutions, we evaluate the

thermodynamic potential $\Omega \equiv \langle \mathcal{H}_{\text{MF}} \rangle - TS$,

$$\Omega = E_{\text{cond}} + \sum_{\gamma} \sum_{|E_{\nu}^{(\gamma)}| < E_c} \left[E_{\nu}^{(\gamma)} f(E_{\nu}^{(\gamma)}) \int d\mathbf{r} |u_{\nu}^{(\gamma)}(\mathbf{r})|^2 - k_B T \ln \left(1 + e^{-E_{\nu}^{(\gamma)}/k_B T} \right) \right]. \quad (13)$$

where $E_{\text{cond}} = -\sum_{\gamma, \gamma'} g_{\gamma\gamma'} \int d\mathbf{r} \Phi_{\gamma}^*(\mathbf{r}) \Phi_{\gamma'}(\mathbf{r})$, with $\Phi_{\gamma}(\mathbf{r}) \equiv \sum_{|E_{\nu}^{(\gamma)}| < E_c} u_{\nu}^{(\gamma)}(\mathbf{r}) v_{\nu}^{(\gamma)*}(\mathbf{r}) f(E_{\nu}^{(\gamma)})$. The thermodynamic potential in Eq. (13) is calculated for both BCS and FFLO states under a fixed H and T . And the modulation period L in equilibrium is determined so as to minimize $\Omega(Q)$ with respect to the FFLO modulation Q . The other physical quantities are also calculated. The magnetization density is defined as

$$M(z) = M^{(1)}(z) + M^{(2)}(z), \quad (14)$$

where we introduce the magnetization in the γ band as

$$M^{(\gamma)}(z) = \sum_{|E_{\nu}^{(\gamma)}| < E_c} \left[|u_{\nu}^{(\gamma)}(z)|^2 f(E_{\nu}^{(\gamma)}) - |v_{\nu}^{(\gamma)}(z)|^2 f(-E_{\nu}^{(\gamma)}) \right]. \quad (15)$$

B. Analytic derivation of critical field H_{c2}

The boundary between normal and superconducting states, $H_{c2}(T)$, can be analytically derived in multi-band systems. The FF and LO states are energetically degenerate on the boundary. Therefore, to determine the $H_{c2}(T)$ line, we assume the pair potential $\Delta^{(\gamma)}(\mathbf{r})$ to be the FF state, which is given by

$$\Delta^{(\gamma)}(z) = \tilde{\Delta}^{(\gamma)} e^{iQz}, \quad (16)$$

where $\tilde{\Delta}^{(\gamma)} = \tilde{\Delta}^{(\gamma)}(H, T) (\in \mathbb{R})$ is a constant and Q denotes the modulation wavenumber of the FF state.

The BdG equation (7) can be transformed to the particle-hole symmetrized form,

$$\underline{K}^{(\gamma)}(z) \varphi_{\nu}^{(\gamma)}(z) = \tilde{E}_{\nu}^{(\gamma)} \varphi_{\nu}^{(\gamma)}(z), \quad (17)$$

where $\tilde{E}_{\nu}^{(\gamma)} = E_{\nu}^{(\gamma)} + \mu_B^{(\gamma)} H$ and

$$\underline{K}^{(\gamma)}(z) = \varepsilon^{(\gamma)}(z) \underline{\sigma}_z + \underline{\sigma}_x e^{-iQz} \underline{\sigma}_z \tilde{\Delta}^{(\gamma)}. \quad (18)$$

The symmetrized BdG matrix (18) satisfies $\underline{\mathcal{C}} \underline{K}^{(\gamma)}(z) \underline{\mathcal{C}}^{-1} = -\underline{K}^{(\gamma)}(z)$ with $\underline{\mathcal{C}} = -i \underline{\sigma}_y K$, where K is the complex conjugate operator. This implies that the positive energy solution $\tilde{E}_{\nu}^{(\gamma)} > 0$ with $[u_{\nu}^{(\gamma)}(z), v_{\nu}^{(\gamma)}(z)]^T$ in Eq. (17) is mapped to the negative energy solution $\tilde{E}_{\nu}^{(\gamma)} < 0$ with $\underline{\mathcal{C}} \varphi_{\nu}^{(\gamma)}(z)$. Then the gap equation (9) is reduced to

$$\Delta^{(\gamma)}(z) \simeq \sum_{\gamma'} g_{\gamma\gamma'} \sum_{0 < \tilde{E}_{\nu}^{(\gamma')} < E_c} u_{\nu}^{(\gamma')}(z) v_{\nu}^{(\gamma')*}(z) \times \left[f(\tilde{E}_{\nu}^{(\gamma')} - \mu_B H) - f(-\tilde{E}_{\nu}^{(\gamma')} - \mu_B H) \right], \quad (19)$$

where $E_c \gg \mu_B H$ is considered for the upper bound for the summation.

We carry out the $U(1)$ transformation of the quasiparticle wavefunction as $\tilde{\varphi}_\nu^{(\gamma)}(z) = [\tilde{u}_\nu^{(\gamma)}(z), \tilde{v}_\nu^{(\gamma)}(z)]^T = \underline{U}(Q)\varphi_\nu^{(\gamma)}(z)$, where $\underline{U}(Q) = \exp[-i(Q/2)z\sigma_z]$. The $U(1)$ transformation reduces the BdG matrix (18) to $\tilde{\underline{K}}^{(\gamma)}(z, Q) = \underline{U}(Q)\underline{K}^{(\gamma)}(z)U^\dagger(Q)$. The transformed BdG matrix satisfies $[\tilde{\underline{K}}^{(\gamma)}(z, Q), -i\frac{d}{dz}\mathbb{1}_2] = \underline{0}_2$, where $\underline{0}_n$ is a n -dimensional zero matrix. The operators $\tilde{\underline{K}}^{(\gamma)}(z, Q)$ and $-i\frac{d}{dz}\mathbb{1}_2$ have the simultaneous eigenstates. The eigenstates can be expressed as $\tilde{\varphi}_k^{(\gamma)}(z) = \exp(ikz)\varphi_k^{(\gamma)}/\sqrt{Z}$, where $Z = \int dz$ is constant, and $\varphi_k^{(\gamma)} = [u_k^{(\gamma)}, v_k^{(\gamma)}]^T$ satisfies the normalization condition, $|u_k^{(\gamma)}|^2 + |v_k^{(\gamma)}|^2 = 1$. Then, Eq. (17) is recast into

$$\underline{K}_Q^{(\gamma)}(k)\varphi_k = \tilde{E}^{(\gamma)}(k, Q)\varphi_k, \quad (20)$$

where

$$\underline{K}_Q^{(\gamma)}(k) = \begin{bmatrix} \varepsilon_Q^{(\gamma)}(k) & \tilde{\Delta}^{(\gamma)} \\ \tilde{\Delta}^{(\gamma)} & -\varepsilon_{-Q}^{(\gamma)}(k) \end{bmatrix}, \quad (21)$$

with $\varepsilon_Q^{(\gamma)}(k) = \frac{\hbar^2}{2M_e}(k + \frac{Q}{2})^2 - \mu_\gamma$. Finally, the eigenenergy $\tilde{E}^{(\gamma)}(k, Q)$ is calculated as

$$\tilde{E}^{(\gamma)}(k, Q) = \frac{\hbar^2}{2M_e}kQ \pm \mathcal{E}^{(\gamma)}(k, Q), \quad (22)$$

with

$$\mathcal{E}^{(\gamma)}(k, Q) = \sqrt{\varepsilon_Q^{(\gamma)}(k)\varepsilon_{-Q}^{(\gamma)}(k) + \left(\frac{\hbar^2 k Q}{2M_e}\right)^2 + [\tilde{\Delta}^{(\gamma)}]^2}. \quad (23)$$

The corresponding eigenstates are given as

$$u_k^{(\gamma)} = \sqrt{\frac{1}{2} \left[1 + \frac{\varepsilon_{-Q}^{(\gamma)}(k) + \frac{\hbar^2}{2M_e}kQ}{\tilde{E}^{(\gamma)}(k, Q) - \frac{\hbar^2}{2M_e}kQ} \right]}, \quad (24)$$

$$v_k^{(\gamma)} = \sqrt{\frac{1}{2} \left[1 - \frac{\varepsilon_Q^{(\gamma)}(k) - \frac{\hbar^2}{2M_e}kQ}{\tilde{E}^{(\gamma)}(k, Q) - \frac{\hbar^2}{2M_e}kQ} \right]}. \quad (25)$$

Using these eigenenergies and eigenfunctions, the pair potential (19) becomes

$$\Delta^{(\gamma)}(z) = - \sum_{\gamma'} g_{\gamma\gamma'} \sum_{\tilde{E}^{(\gamma')}}^+ \frac{\Delta^{(\gamma')}(z)}{2Z} \mathcal{F}^{(\gamma')}(k, Q), \quad (26)$$

$$\mathcal{F}^{(\gamma)}(k, Q) = \frac{1 - f_+^{(\gamma)} - f_-^{(\gamma)}}{\mathcal{E}^{(\gamma)}(k, Q)}, \quad (27)$$

where $f_\pm^{(\gamma)} = f(\tilde{E}^{(\gamma)}(k, Q) \pm \mu_B H)$ and $\sum_{\tilde{E}^{(\gamma')}}^+$ means summation in $0 < \tilde{E}^{(\gamma')}(k, Q) < E_c$. During the calculation, positive sign is taken for $\tilde{E}^{(\gamma)}(k, Q)$ in

Eq. (22). Then the reduced gap equation for $\Delta = [\Delta^{(1)}, \Delta^{(2)}, \dots, \Delta^{(N)}]^T$ is expressed in the N -dimensional matrix form as

$$[\mathbb{1}_N - \underline{\mathcal{I}}_N(Q)] \Delta = \mathbf{0}, \quad (28)$$

with $[\underline{\mathcal{I}}_N(Q)]_{\gamma\gamma'} = g_{\gamma\gamma'} \mathcal{I}^{(\gamma')}(Q)$ and $\mathcal{I}^{(\gamma)}(Q) = -\frac{1}{2} \int_{-k_c}^{k_c} \frac{dk}{2\pi} \mathcal{F}^{(\gamma)}(k, Q)$. We here replace $Z^{-1} \sum_{0 < E < E_c}$ by $\int_{-k_c}^{k_c} \frac{dk}{2\pi}$ in the thermodynamic limit. To have a non-trivial set of Δ , we have the condition,

$$\det[\mathbb{1}_N - \underline{\mathcal{I}}_N(Q)] = 0. \quad (29)$$

The analytical phase boundary $H_{c2}(T)$ for N -band system is obtained from Eq. (29) for various Q 's.

In the present paper, we consider the case of $N = 2$. Then, Eq. (29) can be written as

$$\begin{aligned} & \left[1 - g_{11}\mathcal{I}^{(1)}(Q)\right] \left[1 - g_{22}\mathcal{I}^{(2)}(Q)\right] \\ & - g_{12}g_{21}\mathcal{I}^{(1)}(Q)\mathcal{I}^{(2)}(Q) = 0. \end{aligned} \quad (30)$$

To derive the $H_{c2}(T)$ line, we vary Q (> 0) and H (> 0) so as to find the set of parameters (Q, H) which satisfy Eq. (30) under a fixed temperature T . The highest value of H gives the phase boundary $H_{c2}(T)$ at a fixed temperature T . In a similar manner, we derive the BCS-normal boundary from Eq. (30) with $Q = 0$. The point at which two boundaries meet corresponds to the tricritical point, the Lifshitz point “L”.

III. TWO-BAND SYSTEMS WITH A PASSIVE BAND: THE CASE OF $g_{22} = 0$

Let us start from a simplest, yet nontrivial two-band case with a passive band. This corresponds to the case of $g_{22} = 0$ and the intraband interaction in the second band is absent. In such a case, the superconductivity in the second (passive) band is induced by Cooper pair tunneling from the first (active) band through the interband interaction $g_{12} = g_{21}$. We study the phase diagram for various g_{12} 's. This gives a first step to understand the thermodynamic properties of FFLO phases in multi-band superconductors.

Figure 1 shows the phase diagram in an H - T plane for three sets of parameters: (i) The single-band case ($g_{12} = g_{22} = 0$) and two-band cases with a passive band, (ii) $\mathbf{\Gamma} = (g_{12}/g_{11}, g_{22}/g_{11}, \mu_2/\mu_1) = (0.1, 0.0, 0.5)$ and (iii) $\mathbf{\Gamma} = (0.8, 0.0, 0.5)$. Using the self-consistent solutions under the parameter sets of (ii) and (iii), we estimate $\Delta_0^{(2)}/\Delta_0^{(1)}$ as $\Delta_0^{(2)}/\Delta_0^{(1)} \simeq 0.10$ and $\Delta_0^{(2)}/\Delta_0^{(1)} \simeq 0.49$, respectively. The gap amplitude of the γ band at zero temperature and zero magnetic field is denoted by $\Delta_0^{(\gamma)}$.

The inset of Fig. 1 shows the spatial profile of the pair potential $\Delta^{(\gamma)}(z)$ and the magnetization density $M^{(\gamma)}(z)$ at the filled (red) circle in the main frame of Fig. 1 with the parameter set of the case (iii). The pair potential

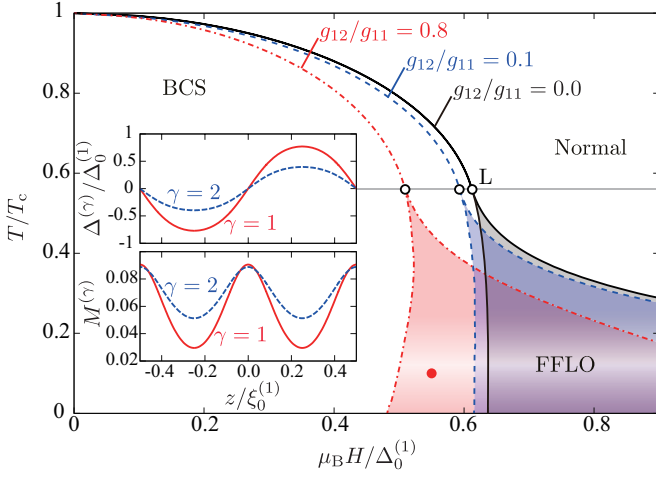


FIG. 1: (color online) Phase diagram for the case of two-band systems with $g_{22} = 0$. (i) The solid (black) line corresponds to the phase boundaries in a single-band superconductor ($g_{12} = g_{22} = 0$), (ii) the dashed (blue) line is the two-band case with a passive band $\mathbf{\Gamma} = (0.1, 0.0, 0.5)$ and (iii) the dash-dotted (red) line is the case of $\mathbf{\Gamma} = (0.8, 0.0, 0.5)$, where $\Delta_0^{(2)}/\Delta_0^{(1)} \simeq 0.10$ (0.49) in the former (latter) case. The temperature of the Lifshitz point, “L”, is a fixed point $T_L/T_c = 0.56 \dots$, which is independent of the interband coupling $g_{12} = g_{21}$. The inset shows the spatial profile of the pair potential in the top row and the magnetization in the bottom row at (T, H) marked as a filled (red) circle in the case (iii). The solid (red) lines and the dashed (blue) lines correspond to the quantities of the first and second band, respectively.

shows that the energy gap of the second band has a finite amplitude, implying that the Cooper pairs are transferred from the active band even if the intraband interaction in the second band is absent. The transferred Cooper pairs also affect back to the electrons in the first band through the Cooper pair tunneling from the passive band. We found the enhancement of the gap amplitude in the first band by increasing the interband interaction.

As shown in Fig. 1, the phase boundary between BCS and FFLO phases shifts to lower fields as the interband interaction increases. It is important to mention that the Lifshitz point, “L”, at which three second-order phase boundaries meet shifts to the lower field as $|g_{12}|$ increases, while the temperature of the Lifshitz point, T_L , is unchanged by the parameter g_{12} . We numerically confirm that T_L is invariant under any parameter changes including intraband interaction g_{22} . It is found that the phase boundary, $H_{LO}(0)$, between BCS and FFLO states, at the zero temperature sharply varies as a function of the interband coupling g_{12} , while the magnetic field of the Lifshitz point, $H_L(T_L)$, is relatively insensitive to g_{12} . This leads to the positive slope of the phase boundary, $dT_{LO}(H)/dH > 0$, in the large interband interaction regime, where $T_{LO}(H)$ is the BCS-FFLO transition line. This feature indicates that the interband interaction stabilizes the FFLO states even in the lower field regime. Note that all the phase boundaries in Fig. 1 are of the

second order.

IV. TWO-BAND SYSTEMS WITH $g_{22} \neq 0$

In this section we set the intraband interaction in the second band to be finite, $g_{22} \neq 0$. In this case, the electrons in both the two bands essentially contribute to the superconducting state and the bands are coherently coupled to each other through the Cooper pair tunneling with $g_{12} = g_{21} \neq 0$. Before going further, let us review the analytic result of the magnetic field H dependence of the FFLO wavenumber Q in a single-band case.¹² By introducing a parameter $k \in [0, 1]$, H and Q are expressed with the analytic form,

$$h(k) \equiv \frac{\mu_B H}{\Delta_0} = \frac{2}{\pi} \frac{E(k)}{k}, \quad (31)$$

$$q(k) \equiv \frac{\hbar v_F Q}{\Delta_0} = \frac{\pi}{kK(k)}, \quad (32)$$

where Δ_0 is the pairing amplitude at $(H, T) = (0, 0)$, v_F is the Fermi velocity, and $K(k)$ and $E(k)$ are the complete elliptic functions of the first and second kinds, respectively.

Although the equations (31) and (32) are derived from a single-band Hamiltonian, it is applicable to a two-band system when the interband coupling $|g_{12}|$ is small. We here define two coherence lengths, $\xi_0^{(\gamma)}$, defined in each electron band,

$$\xi_0^{(\gamma)} k_F^{(\gamma)} = \frac{2\mu_\gamma}{\Delta_0^{(\gamma)}}, \quad (\gamma = 1, 2), \quad (33)$$

where $k_F^{(\gamma)} = \sqrt{2M_e\mu_\gamma/\hbar^2}$ is the Fermi wavenumber of the γ band. Let us here introduce the averaged variables of various quantities. The averaged gap at $(H, T) = (0, 0)$ is $\bar{\Delta}_0 = (\Delta_0^{(1)} + \Delta_0^{(2)})/2$, the averaged chemical potential is $\bar{\mu} = (\mu_1 + \mu_2)/2$, and the averaged coherence length is defined as

$$\bar{\xi} = \frac{\sqrt{2\bar{\mu}}}{\bar{\Delta}_0} \sqrt{\frac{\hbar^2}{M_e}}, \quad (34)$$

where the last equation is analogous to Eq. (33). Using these expressions, $Q^{(\gamma)}$ and $H^{(\gamma)}$ are characterized as,

$$\frac{\mu_B H^{(\gamma)}}{\bar{\Delta}_0} = \frac{\Delta_0^{(\gamma)}}{\bar{\Delta}_0} h(k), \quad (35)$$

$$Q^{(\gamma)} \bar{\xi} = \frac{\Delta_0^{(\gamma)}}{\bar{\Delta}_0} \sqrt{\frac{\bar{\mu}}{\mu_\gamma}} q(k). \quad (36)$$

In this analysis, we can divide the parameter space into the two cases such that the ratio of the FFLO wavenumber in the high field limit denoted as \mathcal{R} is bigger or

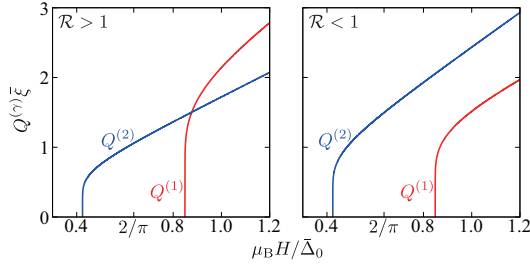


FIG. 2: (color online) Field-dependence of the FFLO modulation number $Q(H)$, based on the single-band analysis. The left (right) figure corresponds to the case $\mathcal{R} > 1$ (< 1).

smaller than 1. From Eqs. (35) and (36), \mathcal{R} is defined as

$$\mathcal{R} \equiv \lim_{\substack{H \rightarrow H_{c2}(0) \\ (k \rightarrow 0)}} \frac{Q^{(1)}}{Q^{(2)}} = \lim_{\substack{H \rightarrow H_{c2}(0) \\ (k \rightarrow 0)}} \frac{dQ^{(1)}/dH^{(1)}}{dQ^{(2)}/dH^{(2)}} = \sqrt{\frac{\mu_2}{\mu_1}}, \quad (37)$$

where $H_{c2}(0)$ is the critical field at $T = 0$. In the present model, $H_{c2}(0)$ diverges.

Without loss of generality, in this paper, we consider $\Delta_0^{(1)} > \Delta_0^{(2)}$ so that $H_{cr}^{(1)} > H_{cr}^{(2)}$, where $H_{cr}^{(\gamma)} = \lim_{k \rightarrow 1} H^{(\gamma)}$ in (35). In such a situation, if $\mathcal{R} > 1$, the curves, $Q^{(1)}(H)$ and $Q^{(2)}(H)$, are crossed at certain H , as shown in the left panel of Fig. 2. For the case of $\mathcal{R} < 1$, $Q^{(1)}(H)$ and $Q^{(2)}(H)$ are never crossed in all H 's as shown in the right panel of Fig. 2. The detailed structures on the two cases, $\mathcal{R} \gtrless 1$, are described in the following two subsections.

A. $\mathcal{R} > 1$ case

1. Phase diagram

Let us consider the $\mathcal{R} > 1$ case where the FFLO modulation wavenumbers $Q^{(\gamma)}$'s in the single-band analysis have a crossing point at a certain magnetic field (left panel of Fig. 2). Using the self-consistent solution of the BdG equation (7) and gap equation (9) with $\Gamma = (0.1, 0.6, 2.0)$, we estimate the ratio of the order parameters at $T = 0$ and $H = 0$ as $\Delta_0^{(2)}/\Delta_0^{(1)} \simeq 0.31$. Then the ratio of the FFLO wavenumber is found to be $\mathcal{R} = \sqrt{2}$. The ground state is determined by minimizing the thermodynamic potential in Eq. (13) with respect to the FFLO modulation period $L = 2\pi/Q$.

The resulting phase diagram is displayed in Fig. 3. In the low temperature regime, the FFLO phase is divided into two regions in terms of Q . In Fig. 3, the phase in the high field regime is referred to as the Q_1 -FFLO phase and in the lower field regime as the Q_2 -FFLO phase. Since the second band has the smaller gap, $|\Delta^{(2)}| < |\Delta^{(1)}|$, the second band becomes passive in the high field regime. The Q_1 -FFLO phase originates from the first band and its field-dependence is understandable with the single-band picture. The detailed structure will be discussed

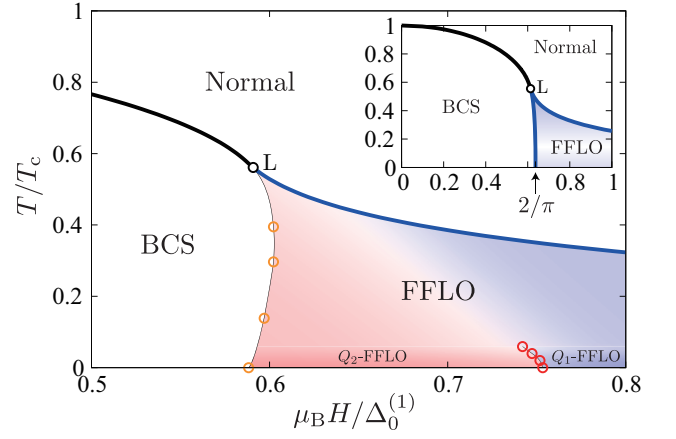


FIG. 3: (color online) Phase diagrams for $\Gamma = (0.1, 0.6, 2.0)$, where $\mathcal{R} = \sqrt{2}$ and $\Delta_0^{(2)}/\Delta_0^{(1)} \simeq 0.31$. The FFLO phase is separated to two regions in the low temperature regime, Q_1 - and Q_2 -FFLO phases. In the high temperature regime, it is ambiguous whether the state is Q_1 - or Q_2 -FFLO. The inset shows the phase diagram for a single-band superconductor.

below. In the lower field regime, however, the gain of the condensation energy in the second band becomes more important, compared with that in the higher field. Since both bands form FFLO states with comparable amplitudes of the pair potentials, each band has the favored FFLO modulation wavenumbers as described in Eqs. (35) and (36). The coherent interband coupling with $g_{12} = g_{21} \neq 0$ induces frustration of two FFLO modulation wavenumbers, $Q^{(1)}$ and $Q^{(2)}$. The competing effect gives rise to emergence of new FFLO phase, that is, the Q_2 -FFLO phase. The frustration is never seen in the case of single-band superconductors and the Q_2 -FFLO is peculiar to multi-band systems. In the high temperature region, the phase boundary between the Q_1 - and Q_2 -FFLO phases is indistinguishable. In Fig. 3, the thick (thin) line indicates the second-order (first-order) phase transition. The BCS, Q_1 -FFLO, and Q_2 -FFLO phases are separated via the first-order phase transition, which is contrast to the second-order BCS-FFLO transition in single-band superconductors.

The thermodynamic potential $\Omega(Q)$ for various H 's is shown in Fig. 4. As H increases, the global minimum of $\Omega(Q)$ shifts from Q_2 -FFLO phases to the Q_1 -FFLO phase. The Q_1 - and Q_2 -FFLO phases are stabilized with either the condition $Q \simeq Q^{(1)}$ or $Q \simeq Q^{(2)}$, respectively. Since $Q^{(1)} \neq Q^{(2)}$, the transition becomes the first order.

It is found that there are many local minima in $\Omega(Q)$ in Fig. 4. To understand the local minima, let us consider the simplified pair potential, $\Delta^{(\gamma)}(z) \propto \sin \tilde{Q}^{(\gamma)} z$. Since two bands are coherently coupled through the interband tunneling, the pair potentials have to satisfy the periodic boundary condition given by Eq. (10) with $\chi = \pi$. Then $\tilde{Q}^{(1)}$ and $\tilde{Q}^{(2)}$ satisfy the condition

$$Q = \tilde{Q}^{(1)}/(2n_1 + 1) = \tilde{Q}^{(2)}/(2n_2 + 1), \quad (38)$$

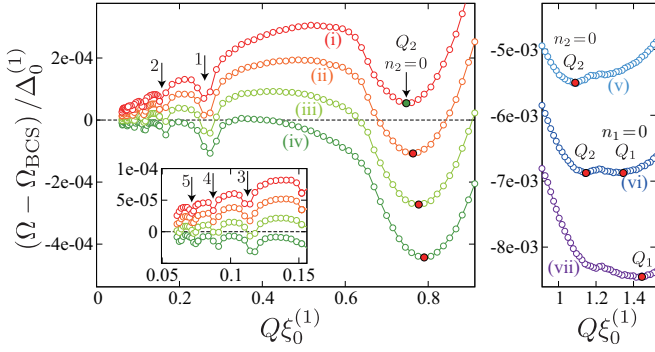


FIG. 4: (color online) Thermodynamic potential Ω as a function of the FFLO modulation wavenumber Q at $T = 0$ for various magnetic fields, $\mu_B H / \Delta_0^{(1)} = 0.586$ (i), 0.591 (ii), 0.597 (iii), 0.602 (iv), 0.726 (v), 0.753 (vi), and 0.780 (vii). The parameters are same as which in Fig. 3. The inset shows the enlarged plot of $\Omega(Q)$ in the smaller Q region. The (red) filled circles show the global minima of $\Omega(Q)$.

with $n_\gamma \in \mathbb{Z}$. In Fig. 4, the local minima in the low Q 's in the low fields correspond to the cases of $n_2 = 1, 2, \dots$ and $n_1 = 0$. In the current case ($\mathcal{R} > 1$), all the states with nonzero n_2 are energetically unstable, relative to the $n_2 = 0$ Q_2 -FFLO state.

2. Pair potentials and local magnetization

Figures 5(a1)-(c1) show the spatial profiles of the pair potentials and Figs. 5(a2)-(c2) are the magnetizations of the ground states under various H 's. Here, Figs. 5(c1) and 5(c2) correspond to the local minimum with the largest Q at the critical field shown in the curve (vi) in Fig. 4. The pair potential and magnetization density of the local minimum with the second largest Q are displayed in (b1) and (b2) of Fig. 5. The data in Figs. 5(a1) and 5(a2) illustrate the global-minimum state with the largest Q in the curve (ii).

To understand the spatial profiles of $\Delta^{(\gamma)}$, we here carry out the Fourier expansion of the pair potential, $\Delta^{(\gamma)}(z) = \sum_{m_\gamma \in \mathbb{N}} \tilde{\Delta}_{m_\gamma}^{(\gamma)} \sin[q_\gamma(2m_\gamma + 1)z]$ where $\mathbb{N} = \{0, 1, 2, \dots\}$. The periodic boundary condition (10) imposes the following condition on q_γ : $Q(2m - 1) = q_1(2m_1 - 1) = q_2(2m_2 - 1)$, where $m, m_\gamma \in \mathbb{N}$ and Q is an FFLO wavenumber. Then the Fourier expansion of the pair potential is given for the first and second bands as

$$\Delta^{(\gamma)}(z) = \sum_{m \in \mathbb{N}} \tilde{\Delta}_m^{(\gamma)} \sin[(2m + 1)Qz]. \quad (39)$$

Due to the symmetry of the pair potential in FFLO states, the Fourier components only take odd numbers, $2m + 1$. The Fourier components of the pair potential is given by

$$\tilde{\Delta}_m^{(\gamma)} = \frac{4}{L} \int_0^{L/2} \Delta^{(\gamma)}(z) \sin[(2m + 1)Qz] dz. \quad (40)$$

Similarly, the magnetization density is expanded in terms of the Fourier series as

$$M^{(\gamma)}(z) = M_{\text{ave}}^{(\gamma)} + \sum_{m \in \mathbb{N}} \tilde{M}_m^{(\gamma)} \cos[2(m + 1)Qz], \quad (41)$$

with an average value of the magnetization,

$$M_{\text{ave}}^{(\gamma)} = \frac{2}{L} \int_0^{L/2} M^{(\gamma)}(z) dz. \quad (42)$$

The Fourier components are given by

$$\tilde{M}_m^{(\gamma)} = \frac{4}{L} \int_0^{L/2} M^{(\gamma)}(z) \cos[2(m + 1)Qz] dz. \quad (43)$$

The Fourier components defined in Eqs. (40) and (43) are displayed in the bottom of Fig. 5. From the Fourier components in Figs. 5(a3)-(c3) and Figs. 5(a4)-(c4), these states are found to be purely sinusoidal states with a single modulation wavenumber Q . The other local minima in Fig. 4 are classified as the Q_2 -FFLO states with $n_2 > 0$. These states can not be the ground state in the case of $\mathcal{R} > 1$, while they have the lowest energy in the case of $\mathcal{R} < 1$. Hence, the detailed structures of the Q_2 -FFLO states with $n_2 > 0$ are described in Sec. IV B.

The Fourier components in Fig. 5 indicate that the pair potentials and the magnetizations are well described with a sinusoidal form with a single FFLO modulation wavenumber. To understand this, let us first clarify the $Q(H)$ curve in the case of a single-band superconductor. In a single-band superconductor, the BCS-FFLO phase transition occurs at the critical field $\mu_B H = (2/\pi)\Delta_0$. The critical field is associated with the one-soliton formation energy and an isolated kink state of $\Delta(z)$ is characterized by $\Delta(z) = \sum_{m \in \mathbb{N}} \tilde{\Delta}_m \sin[Q(2m + 1)z]$ with $\tilde{\Delta}_m = \Delta_0/(2m + 1)$.¹² The higher Fourier components with $m \geq 1$ immediately disappear as H increases and the spatial modulation of Δ results in a sinusoidal form $\Delta(z) \propto \sin(Qz)$. The field dependence of Q in the single-band case is described with Eqs. (31) and (32). The slope of Q with respect to H in the limit of $H \rightarrow \infty$ is obtained as

$$\lim_{H \rightarrow \infty} \frac{\hbar v_F Q / \Delta_0}{\mu_B H / \Delta_0} = \lim_{k \rightarrow 0} \frac{\pi / [kK(k)]}{2E(k) / [\pi k]} = 2. \quad (44)$$

This indicates $Q \sim 2\mu_B H / \hbar v_F$ in the limit of the high magnetic field.

In the case of two-band superconductors with $\Delta_0^{(1)} > \Delta_0^{(2)}$, electrons in the second band feel the relatively high magnetic field even in the vicinity of the phase boundary between BCS to Q_2 -FFLO phases. Therefore, the higher Fourier components never appear. Since pair potentials in two bands are coherently coupled through the inter-band Cooper pair tunneling, the pair potential in the first band is also pulled into a sinusoidal form by the effect of the second band.

Figure 6 shows the field dependence of the FFLO wavenumber Q and the spatially averaged magnetization

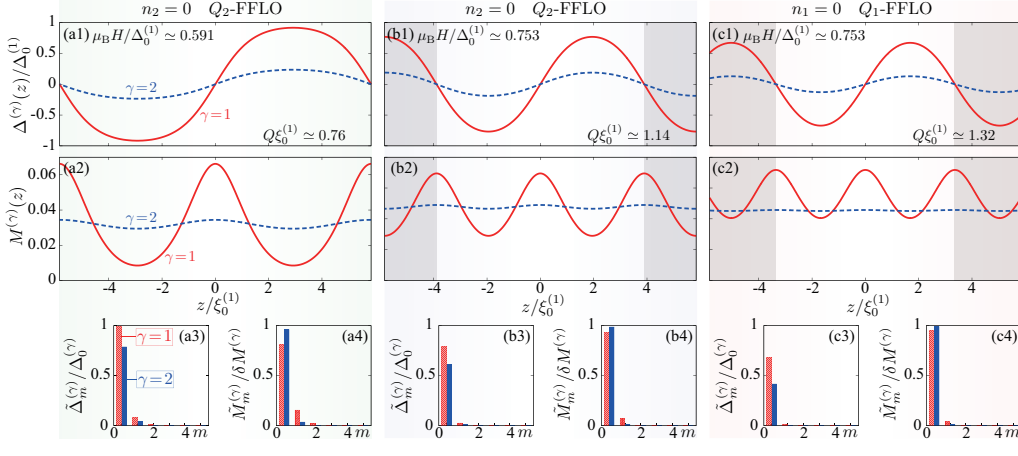


FIG. 5: (color online) Spatial profiles of the gap for $\mu_B H/\Delta_0^{(1)} = 0.591$ (a1), 0.753 (b1), and 0.753 (c1) at $T = 0$. The corresponding magnetization densities are displayed in (a2), (b2), and (c2). (c1) and (c2) correspond to the Q_1 -FFLO state and the others are identified as the Q_2 -FFLO states. The parameters are same as those in Fig. 3. The bottom panels show their Fourier components where $\delta M^{(\gamma)} = \max[M^{(\gamma)}] - M_{\text{ave}}^{(\gamma)}$.

$M_{\text{ave}} \equiv M^{(1)} + M^{(2)}$. The resulting $Q(H)$ curve fits well with the $Q^{(1)}$ and $Q^{(2)}$ curves obtained from the single-band analysis in Eqs. (35) and (36). The ground state in low magnetic field is identified as the Q_2 -FFLO state with $n_2 = 0$ whose $Q(H)$ follows the $Q^{(2)}$ curve, while it turns to the Q_1 -FFLO state with $Q(H) \sim Q^{(1)}(H)$ in the higher field regime. Figure 6 clearly indicates that the transition from Q_2 - to Q_1 -FFLO phases is of the first-order. The transition between BCS to Q_2 -FFLO state is also of the first-order, as shown in Fig. 6. By lowering the magnetic field, the transition occurs and Q drops to zero around $\mu_B H \approx 0.588\Delta_0^{(1)}$.

As shown in Fig. 6, the net magnetization jumps at

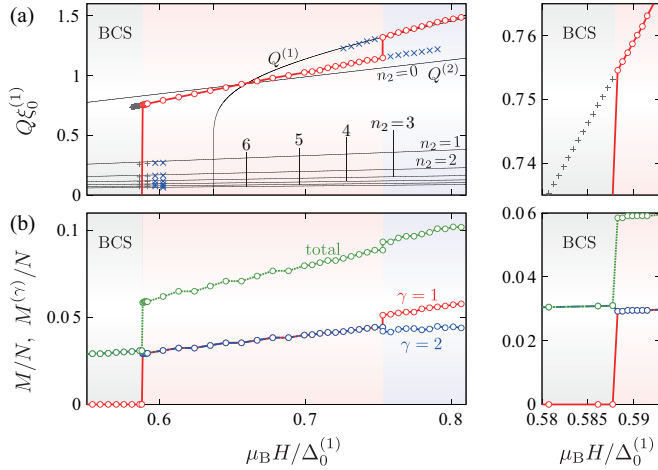


FIG. 6: (color online) (a) FFLO wavenumber Q and (b) spatially averaged magnetization, M and $M^{(\gamma)}$, as a function of H at $T = 0$. The other parameters are same as those in Fig. 3. The (black) thin lines indicate the $Q^{(\gamma)}(H)$ curves obtained from the single-band analysis. The lines at lower Q correspond to the family of the Q_2 -FFLO, $Q^{(2)}/(2n_2 + 1)$, with $n_2 \in \mathbb{N}$. The symbol “ \times ” (“ $+$ ”) indicates the local minimum state whose thermodynamic potential is lower (higher) than that in the BCS state. The right panels show the detailed structures in the lower H region.

each critical field. These jumps manifest the onset of the Q_2 - and Q_1 -FFLO phases and might be observable in experiments. In Fig. 6, it is also found that the net magnetization in the second band decreases at the critical field $\mu_B H \approx 0.75\Delta_0^{(1)}$ between Q_2 - and Q_1 -FFLO phases, while the total magnetization increases. This is also observed in the case of $\mathcal{R} < 1$.

As seen in Fig. 3, the phase boundary between the Q_1 - and Q_2 -FFLO states are indistinguishable in the high temperature region of the phase diagram. This is because the two local minima originated from $Q^{(1)}$ and $Q^{(2)}$ merge into the same value with increasing the temperature, as shown in Fig. 7. The Q_2 -FFLO state with $n_2 = 0$ can be continuously connected to the Q_1 -FFLO state with $n_1 = 0$ if they share the same Q . Note here that, as discussed later, this is different from the case of $\mathcal{R} < 1$ in which the family of the Q_2 -FFLO states with $n_2 > 0$ becomes the ground state and successive

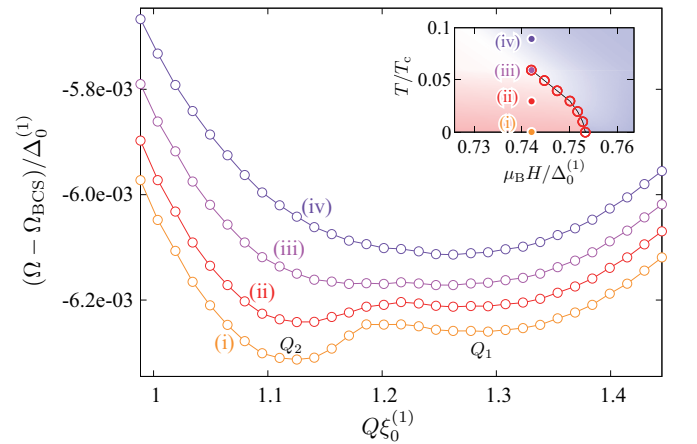


FIG. 7: (color online) Thermodynamic potential Ω as a function of the FFLO modulation wavenumber Q at $\mu_B H/\Delta_0^{(1)} = 0.74$ for various temperatures, $T/T_c = 0$ (i), 0.03 (ii), 0.06 (iii), and 0.09 (iv). Each plot is scaled by $i \times 5 \times 10^{-5}$ ($i = 0, 1, 2, 3$) for visibility. The inset shows the calculated points in the phase diagram in Fig. 3.

first-order transitions occur.

3. Energy spectra and density of states

Let us confirm the realization of the Q_2 -FFLO states from the perspective of the energy spectra. Figure 8 illustrates the energy spectra and the density of states (DOS) of three FFLO states. The corresponding pair potentials are displayed in Fig. 5. The energy spectra in the first and second bands are plotted in Figs. 8(a1) and 8(a2), respectively. The (red) solid line corresponds to the Q_1 -FFLO state and the other lines depict the Q_2 -FFLO states for various H 's. The energy spectrum of the first-band is qualitatively unchanged by the magnetic field, which always opens a finite energy gap at the Fermi level.

The band structures around $E_k = -\mu_B H$ in Figs. 8(a1) and 8(a2) are interpreted as the lattice formation of the Jackiw-Rebbi solitons bound at the FFLO nodes.¹¹ In the case of the Q_2 -FFLO with $n_2 = 0$, as shown in Fig. 8(a2), the energy dispersion of the soliton band does not cross the Fermi level. As H increases, however, the FFLO modulation period $L = 2\pi/Q$ shortens and thus the dispersion of the Jackiw-Rebbi soliton band becomes dispersive. As shown in Fig. 6(a), Q jumps at the critical $\mu_B H/\Delta_0^{(1)} \approx 0.75$ between the Q_2 - and Q_1 -FFLO phases. In the Q_1 -FFLO phase, the Jackiw-Rebbi soliton band crosses the Fermi level. These features are also confirmed in the DOS of the second band (blue lines) displayed in Figs. 8(b1)-(b3), where the zero-energy DOS is absent in the Q_2 -FFLO states in Figs. 8(b2) and 8(b3). The change of low-energy structures implies that the Q_2 -

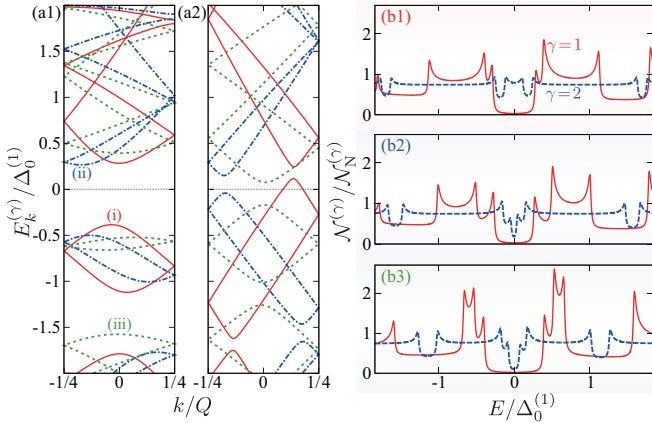


FIG. 8: (color online) Energy spectra of the first band (a1) and the second band (a2). The (red) solid line (i) corresponds to Q_1 -FFLO states at $\mu_B H/\Delta_0^{(1)} = 0.753$. The (blue) dash-dotted line (ii) and the (green) dotted line (iii) correspond to Q_2 -FFLO states with $n_2 = 0$ at $\mu_B H/\Delta_0^{(1)} = 0.753$ and 0.591 , respectively. The density of states in (i)-(iii) are displayed in (b1)-(b3), respectively. The other parameters are same as those in Fig. 3.

FFLO states gain the condensation energy at low temperatures and thus they can be stable relative to the Q_1 -FFLO state.

Since the soliton band is occupied (unoccupied) by only up-spin (down-spin) electrons in the low temperature regime, paramagnetic moments are accumulated by the FFLO nodal planes. Hence, the spatial oscillation of magnetization density in Figs. 5(a2), 5(b2), and 5(c2), reflects the FFLO modulation period L and Jackiw-Rebbi soliton states in the low temperatures, which might be detectable in experiments.

B. $\mathcal{R} < 1$ case

1. Phase diagram

Let us now turn to the case of $\mathcal{R} < 1$ where $Q^{(2)}$ is always bigger than $Q^{(1)}$. The resulting phase diagram is shown in Fig. 9. Here, we take the two sets of parameters: $\Gamma = (0.0625, 0.5, 0.2)$ and $\Gamma = (0.1, 0.6, 0.5)$. Using the former (latter) set, the ratio of the pair potential at $T = 0$ and $H = 0$ is estimated as $\Delta_0^{(2)}/\Delta_0^{(1)} \simeq 0.60$ (0.53). Then the ratio of the wavenumbers is $\mathcal{R} = \sqrt{0.2}$ and $\sqrt{0.5}$, respectively. For both the sets of parameters, the region of high fields and low temperatures is occupied by two FFLO phases, the Q_1 - and Q_2 -FFLO phases. In contrast to the case of $\mathcal{R} > 1$, however, the Q_2 -FFLO phase is further divided into a family of the Q_2 -FFLO states through successive first-order phase transitions. The detailed structures will be discussed below. We here calculate the physical quantities in both the cases, which yield qualitatively same behaviors. In this paper, therefore, we focus on the results with the set of parameters, $\Gamma = (0.0625, 0.5, 0.2)$. The more information of the latter case can be found in Ref. 27.

In Fig. 10 we illustrate the thermodynamic potential Ω for various H 's as a function of the FFLO wavenumber Q . In Fig. 10, the data (i)-(iii) show $\Omega(Q)$ in the vicinity of the phase boundary between the BCS and Q_2 -FFLO phases, and (iv)-(vi) are in the higher field regime around the boundary between Q_2 - and Q_1 -FFLO phases. There exist several local minima in $\Omega(Q)$. In the lower field regime, the FFLO phase with small Q 's can be the ground state, while the value of Q in the ground state successively jumps to larger values with increasing H .

Figures 11(a1)-(c1) show the spatial profile of the pair potentials and the corresponding magnetization densities are displayed in Figs. 11(a2)-(c2). The corresponding Fourier components are displayed in the bottom. As seen in Figs. 11(c1) and 11(c2), the pair potentials of two bands yield a simple sinusoidal modulation, and the spatial oscillations are characterized by a single FFLO modulation wavenumber, corresponding to the Fourier component with $m_\gamma = 0$ in Eq. (40). Similarly, the spatial modulation of $M^{(\gamma)}(z)$ is composed of a single Fourier component with $m = 0$ in Eq. (43). It turns out that the

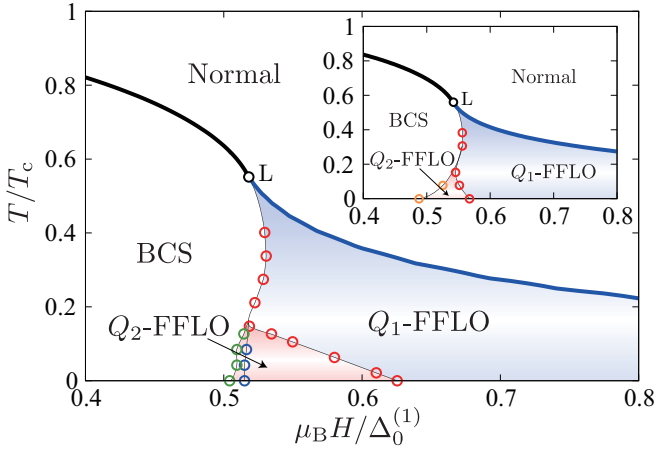


FIG. 9: (color online) Phase diagrams for $\Gamma = (0.0625, 0.5, 0.2)$ in the main frame and for $\Gamma = (0.1, 0.6, 0.5)$ in the inset. The former (latter) case corresponds to $\mathcal{R} = \sqrt{0.2}$ ($\sqrt{0.5}$) and $\Delta_0^{(2)}/\Delta_0^{(1)} \simeq 0.60$ (0.53). The FFLO phase is separated by the first-order transition to Q_1 - and Q_2 -FFLO states. The Q_2 -FFLO phase is divided into a family of the Q_2 -FFLO states through the first-order transitions.

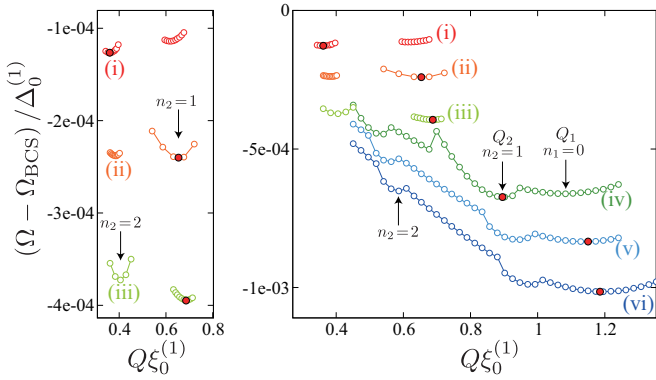


FIG. 10: (color online) Thermodynamic potential $\Omega(Q)$ at $T = 0$ for $\mu_B H / \Delta_0^{(1)} = 0.509$ (i), 0.516 (ii), 0.525 (iii), 0.605 (iv), 0.625 (v), and 0.646 (vi). The set of parameters are $\Gamma = (0.0625, 0.5, 0.2)$. The left panel is an enlarged plot of the low field region. The (red) filled circles denote the global minima of $\Omega(Q)$.

modulation wavenumber Q coincides with the modulation wavenumber favored by the first band, $Q^{(1)}$. In this sense, we refer to this state as the Q_1 -FFLO state. This state corresponds to the local-minimum state with the largest value of Q in Fig. 10. The Q_1 -FFLO state always occupies the high field region of the phase diagram, regardless of $\mathcal{R} > 1$ and $\mathcal{R} < 1$ (see Figs. 3 and 9) and the parameters ($g_{12}/g_{11}, g_{22}/g_{11}$).

2. Pair potentials and local magnetization

Figures 11(b1) and 11(a1) illustrate the spatial profiles of the pair potential which correspond to the local

minima with the second and third largest Q in Fig. 10, respectively. The corresponding magnetization densities are displayed in Fig. 11(b2) and (a2). It is seen from Figs. 11(b3) and 11(a3) that $\Delta^{(\gamma)}(z)$ is composed of multiple wavenumbers, $(2m+1)Q$ ($m = 1, 2, \dots$), in addition to Q . In the case of Fig. 11(b1), the wavenumber $3Q$ of $\Delta^{(\gamma)}(z)$ is favored by the pair potential of the second band $\Delta^{(2)}$, namely, $3Q \simeq Q^{(2)}$. Since the two bands are coherently coupled through the inter-band Cooper pair tunneling and $\Delta^{(1)}$ favors the relatively longer modulation period, the extra Fourier component with Q then mixes the longer modulation period in $\Delta^{(\gamma)}(z)$, which is favored by the first band $\Delta^{(1)}$. As a result, the spatial modulation of Fig. 11(b1) is described as $\Delta^{(\gamma)}(z) \approx \tilde{\Delta}_0^{(\gamma)} \sin(Q^{(2)}z/3) + \tilde{\Delta}_1^{(\gamma)} \sin(Q^{(2)}z)$. We refer to this state as the Q_2 -FFLO state with $n_2 = 1$ (see Fig. 10). Similarly, $\Delta^{(\gamma)}(z)$ in the case of Fig. 11(a1) is composed of mainly two Fourier components, Q and $5Q$, where the shorter period $5Q \simeq Q^{(2)}$ is favored by the second band. The FFLO state in Fig. 11(a1) is identified as the Q_2 -FFLO state with $n_2 = 2$.

Note that in low temperatures, the modulation of the magnetization density reflects the spatial oscillation of $\Delta^{(\gamma)}(z)$ in the FFLO states. As seen in Fig. 11(c4), the spatial modulation of the magnetization density in the Q_2 -FFLO state is expressed by a single Fourier component with $2Q$. In Fig. 11(b4) and (a4), we show the Fourier components of $M^{(\gamma)}(z)$ in Q_2 -FFLO states with $n_2 = 2$ and $n_2 = 1$, where the spatial modulation consists of multiple Fourier components. This feature in Q_2 -FFLO states is qualitatively different from the single- Q behavior in the Q_1 -FFLO state. Hence, the multiple- Q modulations in the magnetization density manifest the stability of the Q_2 -FFLO states.

Let us now consider the transition from Q_2 - to Q_1 -FFLO states. The field-dependence of the FFLO modulation wavenumber, Q , is displayed in Fig. 12(a). The corresponding phase diagram in Fig. 9 indicates that in the higher magnetic field regime, the Q_1 -FFLO state is a ground state. This is because the minority pair potential, $\Delta^{(2)}$, becomes passive in the high field regime and the FFLO modulation is determined by the majority band. Hence, the field-dependence of Q follows the curve $Q^{(1)}(H)$ which is obtained from the single-band analysis in Eqs. (35) and (36). In the lower field regime where the pair potential in the second band is competitive to that of the first band, the frustration between $Q^{(1)}$ and $Q^{(2)}$ gives rise to anomalous field-dependence of the FFLO modulation wavenumber Q . In the case of $\mathcal{R} < 1$ which we consider, the FFLO wavenumber favored by the second-band, $Q^{(2)}$, is always larger than $Q^{(1)}$, as shown in Fig. 2(b). Hence, as discussed above, the lower field region is occupied by a family of the Q_2 -FFLO states, whose pair potentials are characterized by multiple wavenumbers, $(2m+1)Q$ ($m = 0, 1, \dots$), with $Q \simeq Q^{(2)}/(2n_2+1)$. As illustrated in Fig. 12(a), the magnetic field drives successive first-order phase transition among Q_2 -FFLO phases with different n_2 's, which

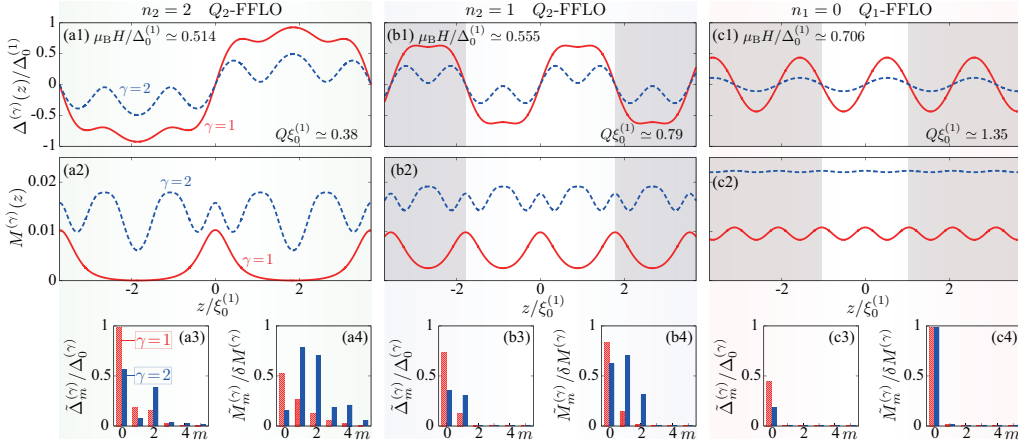


FIG. 11: (color online) Spatial profiles of the gap for $\mu_B H/\Delta_0^{(1)} = 0.514$ (a1), 0.555 (b1), and 0.706 (c1) at $T = 0$. The corresponding magnetization densities are displayed in (a2), (b2), and (c2). (c1) and (c2) correspond to the Q_1 -FFLO state. (a1) and (a2) illustrate the Q_2 -FFLO states with $n_2 = 2$ and (b1) and (b2) correspond to the Q_2 -FFLO states with $n_2 = 1$. The parameters are same as which in Fig. 9. The bottom panels show their Fourier components where $\delta M^{(\gamma)} = \max[M^{(\gamma)}] - M_{\text{ave}}^{(\gamma)}$.

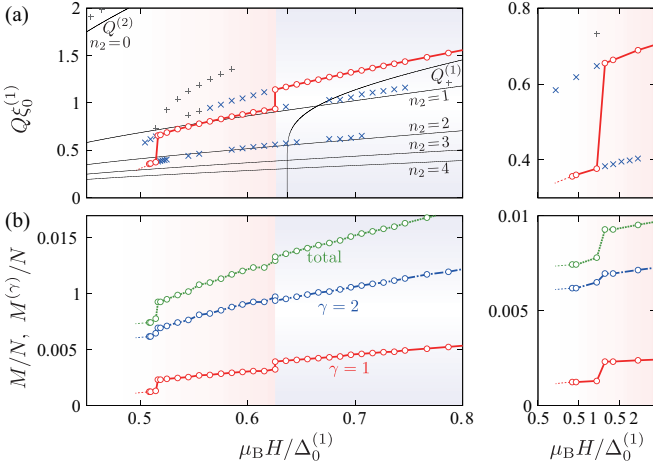


FIG. 12: (color online) (a) FFLO wavenumber Q and (b) spatially averaged magnetizations M and $M^{(\gamma)}$ as a function of H for $\Gamma = (0.0625, 0.5, 0.2)$ and $T = 0$. The (black) thin lines indicate the $Q(H)$ curve obtained from the single-band analysis. We also depict the curves $Q_2(H)/(2n_2+1)$, corresponding to the family of the Q_2 -FFLO. The symbol “ \times ” (“ $+$ ”) denotes the local minimum state whose thermodynamic potential is lower (higher) than that in the BCS state. The right panels illustrate the detailed structures in the lower H region.

are accompanied by the jump of the Q value. The transition from Q_2 - to Q_1 -FFLO phases is also of the first-order. As seen in Fig. 12, the field-dependence of the net magnetization clearly indicates the successive first-order transitions. The so-called *devil's staircase*^{37,38} is peculiar to FFLO phases in multi-band superconductors and might be detectable in experiments.

Note that although there exist more steps in the $\mu_B H/\Delta_0^{(1)} \lesssim 0.5$ of Fig. 12(b), further calculations in the lower field region are technically difficult. This is because Q_2 -FFLO states with an infinitely large n_2 are competing to the spatially uniform BCS state. We find that the

thermodynamic potential of the BCS state is still higher than that of Q_2 -FFLO states around $\mu_B H/\Delta_0^{(1)} \sim 0.5$. Therefore, the critical field below which the BCS state is stabilized will be located in the region of $H_p^{(2)} \lesssim H \lesssim 0.5\Delta_0^{(1)}/\mu_B$, where $H_p^{(2)} = \frac{1}{\sqrt{2}} \frac{\Delta_0^{(2)}}{\mu_B}$ denotes the Pauli-limiting field in the second band and $\mu_B H_p^{(2)}/\Delta_0^{(1)} \simeq 0.42$ with the parameters of Fig. 12.

3. Energy spectra and density of states

Finally, to explain the thermodynamic stability of Q_2 -FFLO states relative to the Q_1 -FFLO state, we illustrate in Fig. 13 the quasiparticle energy spectra and DOS of the Q_1 -FFLO state and Q_2 -FFLO states with $n_2 = 1$ and $n_2 = 2$. Similarly with the case of $\mathcal{R} > 1$ in Sec. IV A, the dispersion of the Q_1 -FFLO state crosses the Fermi level, while the Q_2 -FFLO states open a finite energy gap around the Fermi level.

In the case of the $n_2 = 2$ Q_2 -FFLO state, as shown in Fig. 11(a3), $\Delta^{(\gamma)}(z)$ is composed of two modulation periods $2\pi/Q$ and $2\pi/(5Q)$, $\Delta^{(\gamma)}(z) \approx \tilde{\Delta}_0^{(\gamma)} \sin(Qz) + \tilde{\Delta}_2^{(\gamma)} \sin(5Qz)$. The FFLO state with the short period $2\pi/(5Q)$ is accompanied by a finite zero energy density of states.¹² The mixing of the Fourier component with the longer modulation period $2\pi/Q$, however, folds back the original band into the small reduced Brillouin zone with the $1/5$ size. As a result, the band gap opens around the Fermi level in the reduced Brillouin zone of the minor band (Fig. 13(a2)), resulting in the gain of condensation energy. The multiple-band structure appears around $E \sim -0.2\Delta_0^{(1)}$, $\mu_B H$, and $-\Delta_0^{(1)}$ in the Q_2 -FFLO states with $n_2 = 1$ and $n_2 = 2$. This helps the stability of the Q_2 -FFLO states in the lower field regime, compared with the Q_1 -FFLO state with a finite zero energy DOS.

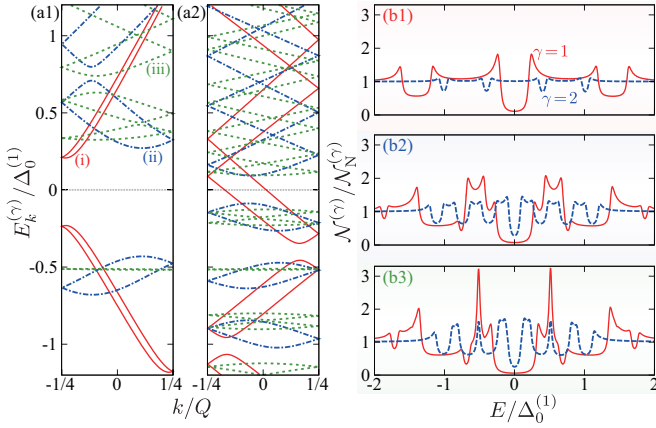


FIG. 13: (color online) Energy spectra of the first band (a1) and the second band (a2) for $\Gamma = (0.0625, 0.5, 0.2)$. The (red) line (i) corresponds to Q_1 -FFLO states at $\mu_B H/\Delta_0^{(1)} = 0.706$. The (blue) dash-dotted line (ii) and (green) dotted line (iii) illustrate the Q_2 -FFLO states with $n_2 = 1$ at $\mu_B H/\Delta_0^{(1)} = 0.555$ and with $n_2 = 2$ at 0.514, respectively. The corresponding density of states to the cases (i)-(iii) are displayed in (b1)-(b3).

V. CONCLUSIONS

We have studied multi-band effects on superconductivity under an external magnetic field. We have here focused on Fulde-Ferrell-Larkin-Ovchinnikov (FFLO) states in two-band systems. Extending the basic theory based on the Bogoliubov-de Gennes equation to a multi-band system, we have developed the formalism to calculate analytic phase boundaries between superconducting states and the normal state.

We have first examined the phase diagram in a two-band system with a passive band, where intraband interaction in the second band is absent. As the interband interaction increases, the critical field, $H_{LO}(T)$, above which the FFLO state is stable, decreases and becomes lower than the tricritical Lifshitz point. This indicates that the BCS-FFLO phase boundary line $T_{LO}(H)$ yields a positive slope, $dT_{LO}(H)/dH > 0$, contrast to that in a single-band superconductor, $dT_{LO}(H)/dH < 0$.¹² We have numerically checked that the temperature at the Lifshitz point is invariant with respect to interband and intraband interactions.

For a two-band superconductor where intraband interactions are present in both bands, there are two different FFLO modulation wavenumbers, $Q^{(1)}$ and $Q^{(2)}$, which are favored by the first and second bands, respectively. The competing effect between two length scales $2\pi/Q^{(1)}$ and $2\pi/Q^{(2)}$ plays an important role in the FFLO states of multi-band superconductors, giving rise to the existence of two FFLO phases: Q_1 -FFLO and Q_2 -FFLO phases. In this paper, we divide the parameter region into two cases: $\mathcal{R} \equiv \lim_{H \rightarrow H_{c2}(0)} Q^{(1)}/Q^{(2)} > 1$ and $\mathcal{R} < 1$. In both cases, it has been demonstrated that the phase

diagram in the low temperature and high field region is occupied by the Q_1 -FFLO phase, whereas the Q_2 -FFLO becomes stable in the lower field regime around the Pauli-limiting fields. In the case of $\mathcal{R} > 1$, the spatial modulation of the pair potential in the Q_1 and Q_2 -FFLO phases is well characterized by a single modulation wavenumber $Q \simeq Q^{(1)}(H)$ and $Q \simeq Q^{(2)}(H)$, respectively. The transition from the BCS to Q_2 -FFLO phase is of the first order. With increasing an applied field, the Q_2 -FFLO phase undergoes the first-order transition to the Q_1 -FFLO phase in the low temperature regime, while the transition becomes ambiguous in high temperatures. In the case of $\mathcal{R} < 1$, the Q_2 -FFLO phase is divided into a family of the Q_2 -FFLO states, where the FFLO modulation is composed of multiple wavenumbers. The transitions between all the superconducting phases are of the first order. The field-dependence of the FFLO modulation wavenumber and net magnetization is accompanied by the devil's staircase, which clearly indicates the successive first-order transitions between the Q_2 -FFLO substates.

Recently, strong Pauli-limited superconductivity has been reported in an Iron-based superconductor, KFe_2As_2 .^{20,23} It is known that KFe_2As_2 has α -, β -, ζ -, and ϵ -bands, where the ϵ -band has a relatively larger Fermi velocity than that in other bands and $\Delta_0^{(\epsilon)} > \Delta_0^{(\alpha)} \sim \Delta_0^{(\beta)} \sim \Delta_0^{(\zeta)}$.³⁹ The FFLO modulation wavenumbers in each band are estimated as $Q^{(\alpha)} \sim Q^{(\beta)} \sim Q^{(\zeta)} < Q^{(\epsilon)}$.²⁷ This corresponds to the case of $\mathcal{R} > 1$ in the present context. Hence, it is inferred that the Q_2 -FFLO phase appears in the low temperature and high field regime and with increasing the magnetic field, it undergoes the first-order transition to the Q_1 -FFLO phase. Note that the generalized WHH approach recently makes the Pauli-limit effect of KFe_2As_2 questionable.⁴⁰ To fully understand the phase diagram of KFe_2As_2 , however, we must take account of orbital depairing effect which induces vortices. In a single-band superconductor, the formation of vortices is competitive to the stability of the FFLO state.^{15,33,41–45} The study on the interplay of vortices with Q_1 - and Q_2 -FFLO states remains in the future work.

Acknowledgments

This work was supported by JSPS (Nos. 21340103, 23840034, 25287085, and 25800199) and by Grant-in-Aid for Scientific Research from MEXT of Japan, “Topological Quantum Phenomena” Nos. 22103005 and 25103716.

Appendix A: BdG equation

In this Appendix, we describe the details on the derivation of the BdG equation (7) and gap equation (9). Let us start from the second-quantized microscopic Hamiltonian with multiple bands under a uniform external magnetic

field, which is presented in Eqs. (3)-(5). Employing the mean field approximation, the Hamiltonian reduces to

$$\mathcal{H}_{\text{int}} \simeq E_{\text{cond}} + \sum_{\gamma} \int d\mathbf{r} \left[\Delta^{(\gamma)*}(\mathbf{r}) \psi_{\downarrow}^{(\gamma)}(\mathbf{r}) \psi_{\uparrow}^{(\gamma)}(\mathbf{r}) + \text{h.c.} \right] \quad (\text{A1})$$

where $E_{\text{cond}} = -\sum_{\gamma, \gamma'} g_{\gamma\gamma'}^{-1} \int d\mathbf{r} \Delta^{(\gamma')*}(\mathbf{r}) \Delta^{(\gamma)}(\mathbf{r})$. Here, $\Delta^{(\gamma)}$ denotes the pair potential defined by

$$\Delta^{(\gamma)}(\mathbf{r}) \equiv \sum_{\gamma'} g_{\gamma\gamma'} \left\langle \psi_{\downarrow}^{(\gamma')}(\mathbf{r}) \psi_{\uparrow}^{(\gamma')}(\mathbf{r}) \right\rangle. \quad (\text{A2})$$

From now on, without loss of generality, \mathbf{H} is fixed to the z axis: $\mathbf{H} = (0, 0, H)$. The second term of Eq. (6) becomes $-\mu_{\text{B}}^{(\gamma)} H \sigma^z$, and the single-particle Hamiltonian density (6) becomes diagonal.

It is convenient to introduce the following spinor notation: $\Psi^{(\gamma)}(\mathbf{r}) = [\psi_{\uparrow}^{(\gamma)}(\mathbf{r}), \psi_{\downarrow}^{(\gamma)\dagger}(\mathbf{r})]^T$, where T means transposition. The mean-field Hamiltonian in Eq. (A1) is rewritten as follows:

$$\mathcal{H}_{\text{MF}} = E'_{\text{cond}} + \sum_{\gamma} \int d\mathbf{r} \Psi^{(\gamma)\dagger}(\mathbf{r}) \underline{\mathcal{K}}^{(\gamma)}(\mathbf{r}) \Psi^{(\gamma)}(\mathbf{r}), \quad (\text{A3})$$

where the BdG Hamiltonian density is given by

$$\underline{\mathcal{K}}^{(\gamma)}(\mathbf{r}) = \begin{bmatrix} \varepsilon^{(\gamma)}(\mathbf{r}) - \mu_{\text{B}}^{(\gamma)} H & \Delta^{(\gamma)}(\mathbf{r}) \\ \Delta^{(\gamma)*}(\mathbf{r}) & -\varepsilon^{(\gamma)}(\mathbf{r}) - \mu_{\text{B}}^{(\gamma)} H \end{bmatrix}. \quad (\text{A4})$$

We introduce the following Bogoliubov transformation,

$$\begin{aligned} \Psi^{(\gamma)}(\mathbf{r}) &= \sum_{\nu} \underline{U}_{\nu}^{(\gamma)}(\mathbf{r}) \boldsymbol{\eta}_{\nu}^{(\gamma)} \\ &= \sum_{\nu} \begin{bmatrix} u_{\nu}^{(\gamma)}(\mathbf{r}) & -v_{\nu}^{(\gamma)*}(\mathbf{r}) \\ v_{\nu}^{(\gamma)}(\mathbf{r}) & u_{\nu}^{(\gamma)*}(\mathbf{r}) \end{bmatrix} \boldsymbol{\eta}_{\nu}^{(\gamma)}, \end{aligned} \quad (\text{A5})$$

with quasiparticle basis, $\boldsymbol{\eta}_{\nu}^{(\gamma)} = [\eta_{\uparrow, \nu}^{(\gamma)}, \eta_{\downarrow, \nu}^{(\gamma)\dagger}]^T$. With the transformation, the mean-field Hamiltonian (A4) with the BdG matrix is diagonalized to

$$\mathcal{H}_{\text{MF}} = E'_{\text{cond}} + \sum_{\sigma, \nu, \gamma} E_{\sigma, \nu}^{(\gamma)} \eta_{\sigma, \nu}^{(\gamma)\dagger} \eta_{\sigma, \nu}^{(\gamma)}. \quad (\text{A6})$$

The creation and the annihilation operators of the quasiparticles, $\eta_{\sigma, \nu}^{(\gamma)\dagger}$ and $\eta_{\sigma, \nu}^{(\gamma)}$, satisfy fermionic anti-commutation relations. The quasiparticle wave function in the matrix form $\underline{U}_{\nu}^{(\gamma)}(\mathbf{r})$ satisfies the orthonormal condition,

$$\int d\mathbf{r} \underline{U}_{\nu}^{(\gamma)\dagger}(\mathbf{r}) \underline{U}_{\nu'}^{(\gamma)}(\mathbf{r}) = \delta_{\nu, \nu'} \mathbf{1}_2, \quad (\text{A7})$$

and the completeness condition,

$$\sum_{\nu} \underline{U}_{\nu}^{(\gamma)}(\mathbf{r}) \underline{U}_{\nu}^{(\gamma)\dagger}(\mathbf{r}') = \delta(\mathbf{r} - \mathbf{r}') \mathbf{1}_2. \quad (\text{A8})$$

By substituting Eq. (A5) to Eq. (A3) and using Eqs. (A6) and (A8), we derive the following Bogoliubov-de Gennes (BdG) equation

$$\underline{\mathcal{K}}^{(\gamma)}(\mathbf{r}) \underline{U}_{\nu}^{(\gamma)}(\mathbf{r}) = \underline{U}_{\nu}^{(\gamma)}(\mathbf{r}) \begin{bmatrix} E_{\uparrow, \nu}^{(\gamma)} & 0 \\ 0 & -E_{\downarrow, \nu}^{(\gamma)} \end{bmatrix}. \quad (\text{A9})$$

The BdG matrix $\underline{\mathcal{K}}^{(\gamma)}(\mathbf{r})$ described above yields double eigenstates for spins. To see this, we set the eigenfunction of up spin states with an eigenvalue $E_{\uparrow, \nu}^{(\gamma)}$ as $\boldsymbol{\varphi}_{\uparrow, \nu}^{(\gamma)}(\mathbf{r}) = [u_{\nu}^{(\gamma)}(\mathbf{r}), v_{\nu}^{(\gamma)}(\mathbf{r})]^T$. Then, the corresponding BdG equation is given by $\underline{\mathcal{K}}^{(\gamma)}(\mathbf{r}) \boldsymbol{\varphi}_{\uparrow, \nu}^{(\gamma)}(\mathbf{r}) = E_{\uparrow, \nu}^{(\gamma)} \boldsymbol{\varphi}_{\uparrow, \nu}^{(\gamma)}(\mathbf{r})$. It is found that the BdG equation (A9) simultaneously has eigenstates for down spins of $\boldsymbol{\varphi}_{\downarrow, \nu}^{(\gamma)}(\mathbf{r}) = [-v_{\nu}^{(\gamma)*}(\mathbf{r}), u_{\nu}^{(\gamma)*}(\mathbf{r})]^T$ with the eigenvalue of $-E_{\downarrow, \nu}^{(\gamma)}$: $\underline{\mathcal{K}}^{(\gamma)}(\mathbf{r}) \boldsymbol{\varphi}_{\downarrow, \nu}^{(\gamma)}(\mathbf{r}) = -E_{\downarrow, \nu}^{(\gamma)} \boldsymbol{\varphi}_{\downarrow, \nu}^{(\gamma)}(\mathbf{r})$. Therefore, once one solves the BdG equation for the quasiparticle $\boldsymbol{\varphi}_{\nu}^{(\gamma)}(\mathbf{r}) = [u_{\nu}^{(\gamma)}(\mathbf{r}), v_{\nu}^{(\gamma)}(\mathbf{r})]^T$ and $E_{\nu}^{(\gamma)}$,

$$\underline{\mathcal{K}}^{(\gamma)}(\mathbf{r}) \boldsymbol{\varphi}_{\nu}^{(\gamma)}(\mathbf{r}) = E_{\nu}^{(\gamma)} \boldsymbol{\varphi}_{\nu}^{(\gamma)}(\mathbf{r}), \quad (\text{A10})$$

then the solution gives the eigenstate for both spin states with positive and negative energies.

One can realize that the BdG equation (A10) is the same form as that in a single band superconductor. Multi-band effects appear through the pair potential $\Delta^{(\gamma)}(\mathbf{r})$. The gap equation is derived by substituting Eq. (A5) to Eq. (A2) and replacing variables in Eq. (A10),

$$\begin{aligned} \Delta^{(\gamma)}(\mathbf{r}) &= \sum_{\gamma', \nu} g_{\gamma\gamma'} \left[u_{\nu}^{(\gamma')}(\mathbf{r}) v_{\nu}^{(\gamma')*}(\mathbf{r}) f(E_{\uparrow, \nu}^{(\gamma')}) \right. \\ &\quad \left. - v_{\nu}^{(\gamma')*}(\mathbf{r}) u_{\nu}^{(\gamma')}(\mathbf{r}) f(-E_{\downarrow, \nu}^{(\gamma')}) \right] \end{aligned} \quad (\text{A11})$$

$$= \sum_{\gamma', \nu} g_{\gamma\gamma'} u_{\nu}^{(\gamma')}(\mathbf{r}) v_{\nu}^{(\gamma')*}(\mathbf{r}) f(E_{\nu}^{(\gamma')}), \quad (\text{A12})$$

where $f(E) = 1/(e^{\beta E} + 1)$ is the Fermi distribution function with inverse temperature $\beta = 1/(k_{\text{B}} T)$ and k_{B} is the Boltzmann constant. Here, we utilize the following relations, $\langle \eta_{\sigma, \nu}^{(\gamma)} \eta_{\sigma', \nu'}^{(\gamma)} \rangle = \langle \eta_{\sigma, \nu}^{(\gamma)\dagger} \eta_{\sigma', \nu'}^{(\gamma)\dagger} \rangle = 0$, $\langle \eta_{\uparrow, \nu}^{(\gamma)\dagger} \eta_{\uparrow, \nu'}^{(\gamma)} \rangle = f(E_{\uparrow, \nu}^{(\gamma)}) \delta_{\nu, \nu'}$, and $\langle \eta_{\downarrow, \nu}^{(\gamma)} \eta_{\downarrow, \nu'}^{(\gamma)\dagger} \rangle = f(-E_{\downarrow, \nu}^{(\gamma)}) \delta_{\nu, \nu'}$. The derived gap equation (A12) has a finite energy cutoff E_c in numerics,

$$\Delta^{(\gamma)}(\mathbf{r}) = \sum_{\gamma'} \sum_{|E_{\nu}^{(\gamma')}| < E_c} g_{\gamma\gamma'} u_{\nu}^{(\gamma')}(\mathbf{r}) v_{\nu}^{(\gamma')*}(\mathbf{r}) f(E_{\nu}^{(\gamma')}). \quad (\text{A13})$$

In the case of a single-band superconductor with a spatially uniform gap Δ_s , the gap equation reduces to

$$\frac{1}{|g_{11}|} = \frac{1}{2\pi} \int_0^{k_c} \frac{dk}{\sqrt{(k^2 - \mu_1)^2 + \Delta_s^2}}, \quad (\text{A14})$$

where $k_c = \sqrt{2M_e E_c / \hbar^2}$. This gives the relation between the cutoff energy and physical quantities such as the intraband coupling constant g_{11} and the pair potential Δ_s at $T = 0$ and $H = 0$. Hence, we estimate the amplitude of the intraband coupling constant g_{11} from Eq. (A14) with the energy cutoff E_c , the chemical potential μ_1 , and the pair potential Δ_s at $T = 0$ and $H = 0$.

Appendix B: Solving the BdG equation with a periodic boundary condition

1. BdG equation with a periodic boundary condition

We start by considering a periodic boundary condition,

$$\Delta(\mathbf{r} + \mathbf{R}) = e^{i\chi(\mathbf{R})} \Delta(\mathbf{r}), \quad (\text{B1})$$

where $\chi(\mathbf{R}) \in \mathbb{R}$. The Bravais lattice vector is defined as $\mathbf{R} = n_1 \mathbf{a}_1 + n_2 \mathbf{a}_2 + n_3 \mathbf{a}_3$ with $n_j \in \mathbb{Z}$ and the primitive vectors of the lattice, \mathbf{a}_j ($j = 1, 2, 3$). We assume that the phase factor $\chi(\mathbf{R})$ yields additivity, $\chi(\mathbf{R}) + \chi(\mathbf{R}') = \chi(\mathbf{R} + \mathbf{R}')$. For simplicity, we do not take account of the local gauge transformation, which implies that $\chi(\mathbf{R})$ is independent of \mathbf{r} .

The BdG equation is

$$\mathcal{H}(\mathbf{r}) \boldsymbol{\varphi}_\mu(\mathbf{r}) = E_\mu \boldsymbol{\varphi}_\mu(\mathbf{r}), \quad (\text{B2})$$

where the matrix is given by

$$\mathcal{H}(\mathbf{r}) = \begin{bmatrix} \epsilon(\mathbf{r}) & \Delta(\mathbf{r}) \\ \Delta(\mathbf{r}) & -\epsilon^*(\mathbf{r}) \end{bmatrix}. \quad (\text{B3})$$

Let us now consider the periodic boundary condition for the BdG equation given by $T_{\mathbf{R}}[\mathcal{H}(\mathbf{r}) \boldsymbol{\varphi}_\mu(\mathbf{r})] = E_\mu T_{\mathbf{R}} \boldsymbol{\varphi}_\mu(\mathbf{r})$, where the translational operator, $T_{\mathbf{R}}$, obeys $T_{\mathbf{R}} T_{\mathbf{R}'} = T_{\mathbf{R}'} T_{\mathbf{R}} = T_{\mathbf{R} + \mathbf{R}'}$. It is obvious from (B1) that the periodicity of the BdG matrix (B3) is expressed as the U(1) gauge transformation, $T_{\mathbf{R}}[\mathcal{H}(\mathbf{r})] = U(\mathbf{R}) \mathcal{H}(\mathbf{r}) U(\mathbf{R})$, where $U(\mathbf{R}) = e^{i\chi(\mathbf{R}) \sigma_z / 2}$ yields additivity, $U(\mathbf{R}) + U(\mathbf{R}') = U(\mathbf{R} + \mathbf{R}')$ and is supposed to be $[U(\mathbf{R})]^4 = 1$. In addition, the eigenfunction of the BdG equation, $\boldsymbol{\varphi}_\mu$, is the simultaneous eigenfunction of the translation operator,

$$[\mathcal{H}(\mathbf{r}), U(\mathbf{R})^\dagger T_{\mathbf{R}}] = 0. \quad (\text{B4})$$

Using the Bloch vector $\mathbf{k} = \frac{m_1}{N_1} \mathbf{b}_1 + \frac{m_2}{N_2} \mathbf{b}_2 + \frac{m_3}{N_3} \mathbf{b}_3$ with the reciprocal lattice vectors $\mathbf{b}_i = 2\pi \epsilon_{ijk} (\mathbf{a}_j \times \mathbf{a}_k) / [\mathbf{a}_i \cdot (\mathbf{a}_j \times \mathbf{a}_k)]$, we obtain the periodic boundary condition on the quasiparticle wavefunction as

$$\boldsymbol{\varphi}_\mu(\mathbf{r} + \mathbf{R}) = U(\mathbf{R}) e^{i\mathbf{k} \cdot \mathbf{R}} \boldsymbol{\varphi}_\mu(\mathbf{r}). \quad (\text{B5})$$

We here impose the Born-von Karman boundary condition, $\boldsymbol{\varphi}_\mu(\mathbf{r} + N_j \mathbf{a}_j) = \boldsymbol{\varphi}_\mu(\mathbf{r})$, where $N_j \in \mathbb{Z}$ and $m_j \in \mathbb{Z}$.

In the current problem, we set $R = L/2$ in Eq. (B1). The phase shift is taken to be $\chi = \pi$ for FFLO states

and $\chi = 2\pi$ for spatially uniform BCS states. Then, the periodic boundary condition on the quasiparticle wavefunction is recast into

$$\boldsymbol{\varphi}_\mu \left(z + \frac{L}{2} \right) = e^{i\mathbf{k} \cdot \mathbf{R}} e^{i\chi \sigma_z / 2} \boldsymbol{\varphi}_\mu(z), \quad (\text{B6})$$

where the Bloch vector is taken to be $\mathbf{k} = 2\pi m \hat{\mathbf{z}} / (LN_L)$ with $N_L \equiv N_j/2$ and $-N_L \leq m < N_L$. We numerically solve the resulting one-dimensional BdG equation with the periodic boundary condition in Eq. (B6) using the finite-element method with the Gauss-Lobatto discrete variable representation

2. Finite element method with the Gauss-Lobatto discrete variable representation

Here we describe the details about how to numerically solve the BdG equation (B2) with the periodic boundary condition in Eq. (B6). In order to map the BdG equation into the eigenvalue equation, we apply the finite (FE) element method implemented with the Gauss-Lobatto discrete variable representation (DVR).⁴⁶

a. Finite-element method with a periodic boundary condition

For simplicity, let us consider the following differential equation in the coordinate space, $q \in [R_L, R_R]$,

$$H(q) \Psi(q) = E \Psi(q). \quad (\text{B7})$$

Without loss of generality, $H(q)$ is composed of spatial derivatives and potential terms as $H(q) = a \frac{d^2}{dq^2} + V(q)$. The eigenfunction $\Psi(q)$ obeys the periodic boundary condition,

$$\Psi(q = R_L) = \mathcal{S} \Psi(q = R_R), \quad (\text{B8})$$

where $\mathcal{S} \in \mathbb{C}$ and $|\mathcal{S}| = 1$.

We start by dividing the continuous variable q into the N intervals, where the i -th interval is defined as $q \in [q_i, q_{i+1}]$ with the $N + 1$ discrete grids $\{q_i\}_{i=0, \dots, N}$ ($q_0 < q_1 < q_2 < \dots < q_N$). Each interval is further divided into sub grids labeled by $\alpha = 1, \dots, M$ as $\{q_\alpha^i\}$ (see Fig. 14). In order to represent wave functions in each interval, we define the set of finite-element basis functions, $\{f_{i,\alpha}(q)\}_{i=1, \dots, N}$, which are identically zero outside a given interval: $f_{i,\alpha}(q) = 0$ for $q \notin [q_i, q_{i+1}]$. The index $\alpha = 1, \dots, M$ denotes the local basis function in each interval and represents the DVR grids.^{47–49} Following Ref. 46, we introduce the boundary condition on

$$f_{i,\alpha=1}(q_i) = 1, \quad f_{i,\alpha=M}(q_{i+1}) = 1, \quad (\text{B9})$$

and for $\alpha = 2, \dots, M - 1$

$$f_{i,\alpha}(q_i) = f_{i,\alpha}(q_{i+1}) = 0. \quad (\text{B10})$$

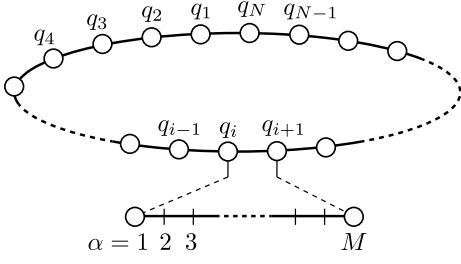


FIG. 14: Grids used in the FE-DVR method.

It is convenient to construct the set of the orthonormal basis functions, $\{\chi_{i,\alpha}(q)\}$, from $\{f_{i,\alpha}(q)\}$, which obeys the condition,

$$\int_{R_L}^{R_R} \chi_{i,\alpha}^*(q) \chi_{j,\beta}(q) dq = \delta_{i,j} \delta_{\alpha,\beta}. \quad (\text{B11})$$

We expand the eigenfunction $\Psi(q)$ in terms of the basis functions,

$$\Psi(q) = \sum_{i,\alpha} C_{i,\alpha} \chi_{i,\alpha}(q). \quad (\text{B12})$$

Since the eigenfunction must be continuous across each interval, the coefficients for $i = 2, \dots, N-1$ are required to satisfy the following conditions

$$C_{i,M} = C_{i+1,1}, \quad (\text{B13})$$

for $i = 2, \dots, N-1$ and

$$C_{0,\alpha} = \mathcal{S} C_{N,\alpha}. \quad (\text{B14})$$

This indicates that the coordinate $q \in [R_L, R_R]$ is divided into $(M-1) \times N+1$ grid points. Each grid q_α^i is accompanied by the local basis functions $\chi_{i,\alpha}(q)$.

b. The Gauss-Lobatto discrete variable representation

We now explicitly define the local basis functions, $\{f_{i,\alpha}(q)\}$, that is, $\{\chi_{i,\alpha}\}$. Following Ref. 46, the DVR is implemented to the finite-element method. The discrete grids in each interval, $\{q_\alpha^i\}$, are chosen to be a set of Gauss-Lobatto quadrature points.

In the interval of $\bar{q} \in [-1, +1]$, the Gauss-Lobatto quadrature rule turns the integral of an arbitrary function $G(\bar{q})$ over the continuous variable \bar{q} to the summation on the discrete grids \bar{q}_α , $\int_{-1}^{+1} G(\bar{q}) d\bar{q} \approx G(-1)\bar{w}_1 + \sum_{\alpha=2}^{M-1} G(\bar{q}_\alpha)\bar{w}_\alpha + G(+1)\bar{w}_M$, which gives an exact result if the function $G(\bar{q})$ is a polynomial of degree $\leq 2M-3$. In contrast to the Gauss-Legendre quadrature, the end-points are constrained to $\bar{q}_{\alpha=1} = q_i$ and $\bar{q}_{\alpha=M} = q_{i+1}$. The points and weights $(\bar{q}_\alpha, \bar{w}_\alpha)$ are chosen to be the α -th zeroth of the first derivative of the $(M-1)$ -th degree

Legendre polynomials, $dP_M(\bar{q})/d\bar{q}$, and

$$\bar{w}_\alpha = \begin{cases} \frac{2}{M(M-1)}, & \text{for } \alpha = 1, M; \\ \frac{2}{M(M-1)[P_{M-1}(\bar{q}_\alpha)]^2}, & \text{otherwise.} \end{cases} \quad (\text{B15})$$

Using the Gauss-Lobatto quadrature points and weights, we now define the grid points q_α^i and the weights w_α^i in each interval as

$$q_\alpha^i = \frac{(q_{i+1} - q_i)\bar{q}_\alpha + (q_{i+1} + q_i)}{2}, \quad (\text{B16})$$

$$w_\alpha^i = \frac{q_{i+1} - q_i}{2} \bar{w}_\alpha. \quad (\text{B17})$$

Now let us construct the DVR basis functions based on the Gauss-Lobatto quadrature, where arbitrary functions given at each FE-DVR grids $\{q_\alpha^i\}$ are interpolated by Lagrange polynomials,

$$f_{i,\alpha}(q) = \begin{cases} \prod_{\beta \neq \alpha} \frac{q - q_\beta^i}{q_\alpha^i - q_\beta^i}, & q_i \leq q \leq q_{i+1}; \\ 0, & q \notin [q_i, q_{i+1}]. \end{cases} \quad (\text{B18})$$

The set of the basis functions is localized at each FE-DVR grid,

$$f_{i,\alpha}(q_\beta^j) = \delta_{i,j} \delta_{\alpha,\beta}, \quad (\text{B19})$$

and obeys the orthogonal condition with the accuracy of the Gauss-Lobatto quadrature, $\int_{R_L}^{R_R} f_{i,\alpha}(q) f_{j,\beta}(q) dq \approx w_\alpha^i \delta_{i,j} \delta_{\alpha,\beta}$.

We can now construct the set of orthonormal functions, $\{\chi_{i,\alpha}(q)\}$, from the local basis functions, $\{f_{i,\alpha}(q)\}$, which allows to expand the eigenfunction $\Psi(q)$. The basis functions are continuous in each interval, $q \in [q_i, q_{i+1}]$, while the continuity at the interval boundaries is ensured by introducing the so-called “bridge” function, $\{\chi_{i,\alpha}\}$. The normalized bridge function at the grid $q_\alpha^i = q_1^1$ and q_M^N is defined as

$$\chi_{i,\alpha}(q) = \frac{f_{N,M}(q) + f_{1,1}(q)}{\sqrt{w_M^N + w_1^1}}. \quad (\text{B20})$$

The bridge functions for interval boundaries with $i \neq 1$ and $\alpha = M$ are given by

$$\chi_{i,\alpha}(q) = \frac{f_{i,M}(q) + f_{i+1,1}(q)}{\sqrt{w_M^i + w_1^{i+1}}}. \quad (\text{B21})$$

For each FE-DVR grid except for the boundaries, the orthonormal functions $\chi_{i,\alpha}$ are obtained by normalizing the local basis function $\{f_{i,\alpha}\}$ as

$$\chi_{i,\alpha}(q) = \frac{f_{i,\alpha}(q)}{\sqrt{w_\alpha^i}}. \quad (\text{B22})$$

The set of the functions in Eqs. (B20)-(B22) satisfies the normalization condition in Eq. (B11)

c. Implementation of the FE-DVR method

By expanding the eigenfunction $\Psi(q)$ in terms of the FE-DVR functions $\chi_{i,\alpha}$, as shown in Eq. (B12), the original equation can be mapped onto the eigenvalue problem. Since $\chi_{i,\alpha}$ is localized at each FE-DVR grid, the potential term $V(q)$ is diagonalized as

$$\int_{R_L}^{R_R} \chi_{i,\alpha}(q) V(q) \chi_{j,\beta}(q) dq = \delta_{i,j} \delta_{\alpha,\beta} V(q_\alpha^i). \quad (\text{B23})$$

The matrix elements of the second derivative term for $i = 2, \dots, N-1$ are evaluated in terms of the FE-DVR basis as

$$\begin{aligned} & \int_{R_L}^{R_R} \chi_{i,\alpha}(q) \left(-\frac{d^2}{dq^2} \right) \chi_{j,\beta}(q) dq \\ &= \mathcal{D}_{\alpha\beta}^i \delta_{i,j} + \mathcal{L}_{\alpha,M}^i \delta_{i,j+1} \delta_{\beta,M} + \mathcal{U}_{M,\beta}^i \delta_{i,j-1} \delta_{\alpha,M} \\ &+ \delta_{i,1} \delta_{j,N} \delta_{\beta,M} \tilde{\mathcal{L}}_\alpha + \delta_{i,N} \delta_{j,1} \delta_{\alpha,M} \tilde{\mathcal{U}}_\beta, \end{aligned} \quad (\text{B24})$$

where the diagonal elements for $\alpha = \beta = M$ are given by

$$\begin{aligned} \mathcal{D}_{\alpha,\beta}^i &= \sum_{\beta=1}^M \left[\frac{w_\gamma^i}{W_M^i} f'_{i,M}(q_\gamma^i) f'_{i,M}(q_\gamma^i) \right. \\ &\quad \left. + \frac{w_\gamma^{i+1}}{W_M^i} f'_{i+1,1}(q_\gamma^{i+1}) f'_{i+1,1}(q_\gamma^{i+1}) \right], \end{aligned} \quad (\text{B25})$$

otherwise

$$\mathcal{D}_{\alpha,\beta}^i = \frac{w_\beta^i}{\sqrt{W_\alpha^i W_\beta^i}} f'_{i,\alpha}(q_\alpha^i) f'_{i,\beta}(q_\beta^i). \quad (\text{B26})$$

The other elements are

$$\mathcal{L}_{\alpha,M}^{i \neq 1} = \sum_{\gamma=1}^M \frac{w_\gamma^i}{\sqrt{W_\alpha^i W_M^{i-1}}} f'_{i,\alpha}(q_\gamma^i) f'_{i,1}(q_\gamma^i), \quad (\text{B27})$$

$$\mathcal{U}_{M,\beta}^{i \neq N} = \sum_{\gamma=1}^M \frac{w_\gamma^{i+1}}{\sqrt{W_M^i W_\beta^{i+1}}} f'_{i+1,1}(q_\gamma^{i+1}) f'_{i+1,\beta}(q_\gamma^{i+1}). \quad (\text{B28})$$

and $\mathcal{L}_{\alpha,M}^{i=1} = 0$ and $\mathcal{U}_{M,\beta}^{i=N} = 0$. The elements $\tilde{\mathcal{L}}_\alpha$ and $\tilde{\mathcal{U}}_\beta$ are obtained with the phase factor in Eq. (B8) as

$$\tilde{\mathcal{L}}_\alpha = \mathcal{S} \sum_{\gamma=1}^M \frac{w_\gamma^1}{\sqrt{W_\alpha^1 W_M^N}} f'_{1,\alpha}(q_\gamma^1) f'_{1,1}(q_\gamma^1), \quad (\text{B29})$$

$$\tilde{\mathcal{U}}_\beta = \mathcal{S}^* \sum_{\gamma=1}^M \frac{w_\gamma^1}{\sqrt{W_M^N W_\beta^1}} f'_{1,1}(q_\gamma^1) f'_{1,\beta}(q_\gamma^1). \quad (\text{B30})$$

We here set $W_\alpha^i = w_M^N + w_1^1$ for $(i, \alpha) = (N, M)$ and $(1, 1)$ and $W_\alpha^i = w_M^i + w_1^{i+1}$ for $i \neq 1, N$ and $\alpha = M$, otherwise $W_\alpha^i = w_\alpha^i$. The first derivatives of the local basis functions $f_{i,\alpha}(q)$ at quadrature points, $f'_{i,\alpha}(q_\beta^i) \equiv df_{i,\alpha}(q)/dq|_{q=q_\beta^i}$, are given by

$$f'_{i,\alpha}(q_\beta^i) = \begin{cases} \frac{1}{q_\alpha^i - q_\beta^i} \prod_{\gamma \neq \alpha, \beta} \frac{q_\beta^i - q_\gamma^i}{q_\alpha^i - q_\gamma^i}, & \text{for } \alpha \neq \beta; \\ \frac{1}{2w_\alpha^i} (\delta_{\alpha,M} - \delta_{\alpha,1}), & \text{for } \alpha = \beta. \end{cases} \quad (\text{B31})$$

In the FE-DVR method, non-zero Hamiltonian matrix elements are composed of only the gradient terms and the potential terms is fully diagonalized. The number of non-zero elements, N_{mat} , are determined by the number of DVR grids in each interval, M ; $N_{\text{mat}} \sim M^2$. This drastically reduces the number of non-zero elements in the standard DVR method^{47–49} with $N_{\text{mat}} \sim (NM)^2$. Hence, the FE-DVR method is accompanied by the sparse matrix and convenient for the implementation of the Lanczos/Arnoldi algorithm and massive parallel computation.⁵⁰

* Electronic address: masahiro.takahashi@gakushuin.ac.jp

† Electronic address: mizushima@mp.okayama-u.ac.jp

‡ Electronic address: machida@mp.okayama-u.ac.jp

¹ P. Fulde and R. A. Ferrell, Phys. Rev. **135**, A550 (1964).

² A. I. Larkin and Y. N. Ovchinnikov, Sov. Phys. JETP **20**, 762 (1965).

³ Y. Matsuda and H. Shimahara, J. Phys. Soc. Jpn. **76**, 051005 (2007).

⁴ M. W. Zwierlein, A. Schirotzek, C. H. Schunck, and W. Ketterle, Science **311**, 492 (2006).

⁵ Y. Liao, A. S. C. Rittner, T. Paprotta, W. Li, G. B. Partridge, R. G. Hulet, S. K. Baur, and E. J. Mueller, Nature **467**, 567 (2010).

⁶ T. Mizushima, K. Machida, and M. Ichioka, Phys. Rev. Lett. **94**, 060404 (2005).

⁷ T. Mizushima, M. Ichioka, and K. Machida, J. Phys. Soc.

Jpn. **76**, 104006 (2007).

⁸ D. E. Sheehy and L. Radzihovsky, Ann. Phys. (N. Y.) **322**, 1790 (2007).

⁹ Z. Cai, Y. Wang, and C. Wu, Phys. Rev. A **83**, 063621 (2011).

¹⁰ R. Casalbuoni and G. Nardulli, Rev. Mod. Phys. **76**, 263 (2004).

¹¹ R. Jackiw and C. Rebbi, Phys. Rev. D **13**, 3398 (1976).

¹² K. Machida and H. Nakanishi, Phys. Rev. B **30**, 122 (1984).

¹³ W. P. Su, J. R. Schrieffer, and A. J. Heeger, Phys. Rev. Lett. **42**, 1698 (1979).

¹⁴ H. Takayama, Y. R. Lin-Liu, and K. Maki, Phys. Rev. B **21**, 2388 (1980).

¹⁵ T. Mizushima, K. Machida, and M. Ichioka, Phys. Rev. Lett. **95**, 117003 (2005) and references therein.

- ¹⁶ L. Komendová, Y. Chen, A. A. Shanenko, M. V. Milošević, and F. M. Peeters, Phys. Rev. Lett. **108**, 207002 (2012).
- ¹⁷ Y. Maeno, S. Kittaka, T. Nomura, S. Yonezawa, and K. Ishida, J. Phys. Soc. Jpn. **81**, 011009 (2012).
- ¹⁸ K. Cho, H. Kim, M. A. Tanatar, Y. J. Song, Y. S. Kwon, W. A. Coniglio, C. C. Agosta, A. Gurevich, and R. Prozorov, Phys. Rev. B **83**, 060502(R) (2011).
- ¹⁹ K. Cho, H. Kim, M. A. Tanatar, Y. J. Song, Y. S. Kwon, W. A. Coniglio, C. C. Agosta, A. Gurevich, and R. Prozorov, Phys. Rev. B **83**, 060502(R) (2011).
- ²⁰ P. Burger, F. Hardy, D. Aoki, A. E. Böhm, R. Eder, R. Heid, T. Wolf, P. Schweiss, R. Fromknecht, M. J. Jackson, C. Paulsen, C. Meingast, Phys. Rev. B **88**, 014517 (2013).
- ²¹ T. Terashima, M. Kimata, N. Kurita, H. Satsukawa, A. Harada, K. Hazama, M. Imai, A. Sato, K. Kihou, C.-H. Lee, H. Kito, H. Eisaki, A. Iyo, T. Saito, H. Fukazawa, Y. Kohori, H. Harima, and S. Uji, J. Phys. Soc. Jpn. **79**, 053702 (2010).
- ²² T. Terashima, K. Kihou, M. Tomita, S. Tsuchiya, N. Kikugawa, S. Ishida, C.-H. Lee, A. Iyo, H. Eisaki, and S. Uji, Phys. Rev. B **87**, 184513 (2013).
- ²³ D. A. Zocco, K. Grube, F. Eilers, T. Wolf, H. v. Löhneysen, Phys. Rev. Lett. **111**, 057007 (2013).
- ²⁴ S. Kittaka, Y. Aoki, N. Kase, T. Sakakibara, T. Saito, H. Fukazawa, Y. Kohori, K. Kihou, C.-H. Lee, A. Iyo, H. Eisaki, K. Deguchi, N. K. Sato, Y. Tsutsumi, and K. Machida, J. Phys. Soc. Jpn. **83**, 013704 (2014).
- ²⁵ A. Gurevich, Phys. Rev. B **82**, 184504 (2010).
- ²⁶ A. Ptok and D. Crivelli, J. Low Temp. Phys. **172**, 226 (2013).
- ²⁷ T. Mizushima, M. Takahashi, and K. Machida, J. Phys. Soc. Jpn. in press (arXiv:1305.3678).
- ²⁸ J. Garaud, J. Carlström, and E. Babaev, Phys. Rev. Lett. **107**, 197001 (2011).
- ²⁹ E. Babaev and M. Speight, Phys. Rev. B **72**, 180502(R) (2005).
- ³⁰ J. Carlström, E. Babaev, and M. Speight, Phys. Rev. B **83**, 174509 (2011).
- ³¹ V. G. Kogan and J. Schmalian, Phys. Rev. B **83**, 054515 (2011).
- ³² T. Hirano, K. Takamori, M. Ichioka, and K. Machida, J. Phys. Soc. Jpn. **82**, 063708 (2013).
- ³³ K. M. Suzuki, Y. Tsutsumi, N. Nakai, M. Ichioka, and K. Machida, J. Phys. Soc. Jpn. **80**, 123706 (2011).
- ³⁴ H. Suhl, B. T. Matthias, and L. R. Walker, Phys. Rev. Lett. **3**, 552 (1959).
- ³⁵ S. Yonezawa, S. Kusaba, Y. Maeno, P. Auban-Senzier, C. Pasquier, K. Bechgaard, and D. Jérôme, Phys. Rev. Lett. **100**, 117002 (2008).
- ³⁶ B. Bergk, A. Demuer, I. Sheikin, Y. Wang, J. Wosnitzer, Y. Nakazawa, and R. Lortz, Phys. Rev. B **83**, 064506 (2011).
- ³⁷ P. Bak, Rep. Prog. Phys. **45**, 587 (1982).
- ³⁸ M. Chaikin and T. C. Lubensky, *“Principles of Condensed Matter Physics”* (Cambridge Univ. Press, Cambridge, 1995).
- ³⁹ F. Hardy, R. Eder, M. Jackson, D. Aoki, C. Paulsen, T. Wolf, P. Burger, A. Böhm, P. Schweiss, P. Adelman, R. A. Fisher, and C. Meingast, J. Phys. Soc. Jpn. **83**, 014711 (2014).
- ⁴⁰ V. G. Kogan and R. Prozorov, Rep. Prog. Phys. **75**, 114502 (2012).
- ⁴¹ N. Nakai, M. Ichioka, and K. Machida, J. Phys. Soc. Jpn. **71**, 23 (2002).
- ⁴² M. Ichioka, K. Machida, N. Nakai, and P. Miranović, Phys. Rev. B **70**, 144508 (2004).
- ⁴³ M. Ichioka and K. Machida, Phys. Rev. B **76**, 064502 (2007).
- ⁴⁴ M. Ichioka, H. Adachi, T. Mizushima, and K. Machida, Phys. Rev. B **76**, 014503 (2007).
- ⁴⁵ K. M. Suzuki, M. Ichioka, and K. Machida, Phys. Rev. B **83**, 140503(R) (2011).
- ⁴⁶ T. N. Rescigno and C. W. McCurdy, Phys. Rev. A **62**, 032706 (2000).
- ⁴⁷ J. C. Light, I. P. Hamilton, and J. V. Lill, J. Chem. Phys. **82**, 1400 (1985).
- ⁴⁸ D. Baye and P.-H. Heenen, J. Phys. A: Math. Gen. **19**, 2041 (1986).
- ⁴⁹ D. E. Manolopoulos and R. E. Wyatt, Chem. Phys. Lett. **152**, 23 (1988).
- ⁵⁰ B. I. Schneider, L. A. Collins, and S. X. Hu, Phys. Rev. E **73**, 036708 (2006).